Nonintrusive experimental aeroelastic analysis of a highly flexible wing

Mertens, Christoph; Fernández, José L.Costa; Sodja, Jurij; Sciacchitano, Andrea; Van Oudheusden, Bas W.

Important note
To cite this publication, please use the final published version (if applicable).
Please check the document version above.

Nonintrusive Experimental Aeroelastic Analysis of a Highly Flexible Wing

Christoph Mertens,* José L. Costa Fernández,† Jurij Sodja,‡ Andrea Sciacchitano,§ and
Bas W. van Oudheusden§
Delft University of Technology, 2629 HS Delft, The Netherlands

https://doi.org/10.2514/1.J062476

The aeroelastic response of the Delft–Pazy wing to steady and periodic unsteady inflow conditions is analyzed experimentally. The Delft–Pazy wing is a highly flexible wing model based on the benchmark Pazy wing (Avin, O., Raveh, D. E., Drachinsky, A., Ben-Shmuel, Y., and Tur, M., "Experimental Aeroelastic Benchmark of a Very Flexible Wing," *AIAA Journal*, Vol. 60, No. 3, 2022, pp. 1745–1768) and exhibits wingtip displacements of more than 24% of the span in the present study. The nonintrusive measurements are performed with an integrated optical approach that provides combined measurements of the structural response of the wing and the unsteady flowfield around it. The aeroelastic loads acting on the wing are derived using physical models and validated against force balance measurements, showing a good agreement for all considered inflow conditions. The analysis of the aeroelastic response of the wing to the unsteady inflow produced by a gust generator shows that both structural and aerodynamic responses depend strongly on the frequency of the gust. The results of this study provide a characterization of the aeroelastic behavior of the Delft–Pazy wing and can serve as a reference for the development of novel and improved nonlinear aeroelastic simulation models.

Nomenclature

C_ℓ	=	section lift coefficient
c	=	chord length, m
d	=	distance from the wing, m
F	=	force, N
f	=	frequency, Hz
I	=	inertial force, N
k	=	reduced frequency
L	=	lift, N
N	=	number of integration contours for averaging
s	=	wingspan, m
T	=	period, s
t	=	time, s
U_∞	=	freestream velocity, $m \cdot s^{-1}$
u	=	streamwise velocity component, $m \cdot s^{-1}$
v	=	crossflow velocity component, $m \cdot s^{-1}$
w	=	wing out-of-plane deflection, m
x	=	streamwise coordinate
y	=	crossflow coordinate
z	=	spanwise coordinate
α	=	angle of attack, deg
β	=	gust vane angle, deg
Γ_b	=	bound circulation, m^2/s
Γ_p	=	partial bound circulation, m^2/s
Δ	=	difference
δ	=	residual
ϵ	=	twist angle, deg
μ	=	mass per unit span, $kg \cdot m^{-1}$
ρ	=	air density, kg/m^3
σ	=	standard deviation
Φ	=	phase shift, deg

Subscripts

B	=	balance measurement
e	=	effective
FEM	=	finite element model
GVT	=	ground vibration test
g	=	gust
LE	=	leading edge
TE	=	trailing edge
ref	=	reference
v	=	motion-induced
x	=	streamwise component
y	=	crossflow component

Superscript

′	=	sectional force, per unit span

*Ph.D. Candidate, Flow Physics and Technology Department, Faculty of Aerospace Engineering; C.Mertens@tudelft.nl. Student Member AIAA (Corresponding Author).

†M.Sc. Student, Flow Physics and Technology Department, Faculty of Aerospace Engineering; currently 77550 Moissy-Cramayel, France.

‡Assistant Professor, Aerospace Structures and Materials Department, Faculty of Aerospace Engineering. Senior Member AIAA.

§Associate Professor, Flow Physics and Technology Department, Faculty of Aerospace Engineering.

I. Introduction

A CURRENT trend in aviation is toward the use of more flexible lifting structures, mainly driven by the desire to improve efficiency by saving structural weight. As a consequence, larger structural deformations are observed and aeroelastic effects become more relevant. For very flexible wings, the structural deformation can become so large as to introduce nonlinear aerodynamic and structural effects that violate the assumptions employed in linear aeroelastic prediction models [1]. These effects are amplified in the case of a gust inflow condition, which leads to increased loads on the wing as compared to steady inflow [2]. This problem has motivated the development of novel aeroelastic prediction methods that account for these nonlinear effects on highly flexible structures [3–5]. In the past, significant progress in aeroelastic research has been achieved based on experimental aeroelastic studies that served as a benchmark for the development of improved simulation methods: for example, the case in which structural nonlinearities occurred on high-aspect-ratio wings [6–8]. Following this tradition, a novel experimental benchmark of a highly flexible wing, known as the Pazy wing, has recently been introduced to support the development of numerical prediction models for highly flexible structures with experimental reference data [9]. This wing has been shown to sustain very large

deformations in the wind tunnel, with tip displacements of more than 50% of the span. Previous experimental studies on the Pazy wing were conducted at Technion—Israel Institute of Technology and were focused on the behavior of the wing in steady inflow, during inflow velocity sweeps [9], and on the limit-cycle oscillation behavior of the wing [10]. Several numerical studies have followed these experimental activities, using the results as a benchmark for the validation of numerical models [11–14]. In the present study, an adapted version of the highly flexible Pazy benchmark wing is studied in a wind-tunnel experiment, where the focus is on the experimental characterization of the gust response of the highly flexible wing.

The production of reference data from aeroelastic wind-tunnel experiments is challenging due to the interaction of the three forces comprising Collar's triangle (aerodynamic, inertial, elastic) [15], which should ideally all be fully quantified based on the experimental measurement data. A variety of diagnostics exists to measure the individual physical quantities that allow the determination of each of the forces locally (e.g., pressure transducers, accelerometers, and strain gauges) or in an integral sense by mounting the wing at the root to a load cell or a force balance; however, their coordinated use results in complex setups and expensive experimental models. Additionally, installed sensors are invasive to the experimental model, thus modifying its mass and stiffness distribution as well as typically achieving only a relatively low spatial resolution due to space limitations inside the model. As a result, the experimental reference data from aeroelastic wind-tunnel measurements on flexible wings that are available in the published literature are usually limited to only a few parameters, such as the wingtip deflection or the frequency of the dynamic motion [16]. In the existing experimental studies of the Pazy wing, wind-tunnel measurements were performed with fiber optic strain sensors, an optical motion tracking system, and a force balance, whereas no dedicated aerodynamic measurements were performed [9,10].

Optical measurement techniques (such as photogrammetry [17] for measuring the structural response and particle image or tracking velocimetry [18] for aerodynamic measurements) permit nonintrusive field measurements, and hence overcome many of the limitations associated with the use of installed sensors. On the other hand, the drawback of these nonintrusive techniques is that the determination of the aeroelastic forces from the measured quantities, such as structural displacements or flow velocity, is not straightforward. This topic has therefore been subject to considerable research efforts in recent years [19–21]. Despite this additional effort, the advantages of optical measurement techniques are prevailing; and several recent studies have employed a combination of different optical techniques for characterizing fluid–structure interactions in wind-tunnel experiments [22–24].

A common issue in these studies is tackling the complication of the experimental setup and the data processing that arises from the coordinated use of two different optical measurement systems or techniques to obtain the structural and flow measurements. A measurement approach that does not suffer from this limitation is Lagrangian particle tracking (LPT). It was recently shown that LPT, implemented via the shake-the-box algorithm [25], can form the basis for a single system capable of providing an integrated measurement of the structural displacements and aerodynamic loads on unsteady airfoils on a relatively large scale (wingspan on the order of 1 m) [26]. The structural response is thereby determined by tracking fiducial markers on the surface of the wind-tunnel model, whereas the aerodynamic loads are inferred from flowfield measurements that are conducted by tracking flow tracers with the same measurement. In a recent demonstration study, this approach has been applied to determine the three forces in Collar's triangle acting on a section of a flexible wing in linear aeroelastic conditions [27]. Although the determination of the three forces in the demonstration study was successful, with a sufficient level of accuracy to serve as a proof of concept, the direct relevance of the results of the study for use as benchmark data was limited by two major aspects: the measurement volume size, and the low aeroelastic complexity of the experimental conditions. In Ref. [27], nonintrusive measurements were conducted only for one section of the wing, which means that the loads distribution on the wing had to be estimated; and the experimental aeroelastic conditions were limited to a relatively small angle of attack

of $\alpha = 5$ deg and small deflections of the flexible wing, reaching a maximum tip deflection of only 2% of the wingspan.

These limitations are overcome in the current study, where LPT measurements are used to characterize the aeroelastic response of a highly flexible wing in steady and unsteady inflow conditions. The unsteady inflow conditions considered in this study are produced by a continuous sinusoidal operation of a gust generator. Two different angles of attack and two different excitation frequencies are studied, producing different static and dynamic aeroelastic wing responses, respectively. The design of the investigated Delft–Pazy wing is very similar to the Pazy benchmark wing and exhibits wingtip displacements of up to 25% of the span. This study aims to extend the current state of the art in aeroelastic measurement technology by providing flowfield measurements around the wing along the entire span, combined with structural deformation measurements of the wing, using a single measurement system. The particular relevance of the results of this study for supporting the development of novel aeroelastic prediction methods is determined by the scale of the measurements and the aeroelastic conditions in which these measurements are performed, which include large deflections and the onset of boundary-layer separation.

II. Nonintrusive Loads Determination Methods

In the measurement approach followed in this study, the three different aeroelastic forces are derived from the integrated aeroelastic measurements using appropriate physical principles. The aerodynamic load is determined from the measurements of the flowfield around the wing. The inertial load is derived from the wing shapes that are reconstructed from the position measurements of the surface markers on the wing. The elastic force is evaluated from the other two forces based on the equilibrium of forces acting on the wing.

A. Aerodynamic Load

The aeroelastic response of the wing to the steady and unsteady inflow conditions that are considered in this study is predominantly constituted by the out-of-plane deflection. It follows that the component of the aerodynamic force that predominantly determines the aeroelastic response of the wing is the lift force because, at the considered angles of attack ($\alpha = 5$ deg and $\alpha = 10$ deg; see Sec. III.C), the lift-to-drag ratio is around 35 based on Xfoil [28] calculations and the wing chord is still approximately aligned with the freestream (see Fig. 1), meaning that the lift force contributes more effectively to the out-of-plane deflection. Overall, this means that the lift force contributes approximately 400 times more than the drag force to the out-of-plane deflection at $\alpha = 5$ deg and about 200 times more at $\alpha = 10$ deg. The analysis of the forces in this study is thus limited to the forces acting in the y direction in the wind-tunnel coordinate system, and the drag force is not taken into account.

In steady conditions, the lift per unit span of a wing section is given by the Kutta–Zhukovsky theorem [29]:

$$L' = \rho U_\infty \Gamma_b \tag{1}$$

where ρ is the air density, U_∞ is the freestream velocity, and Γ_b is the bound circulation around the wing section. The value of Γ_b can be obtained from a measured flow velocity field $\boldsymbol{u}$ with a line integral of the velocity over a closed path C enclosing the wing section:
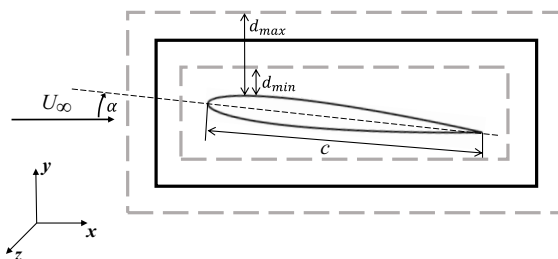

Fig. 1 Wing section with an example rectangular integration contour (black line) and the limits of the range of the different contours (gray dashed lines).

$$\Gamma_b = -\oint_C \boldsymbol{u} \cdot \mathrm{d}s \tag{2}$$

In accordance with potential flow theory, previous experimental studies on viscous flows around airfoils have shown no considerable systematic dependence of the determined circulation on the integration contour C as long as the contour is not placed in the direct vicinity of the airfoil, i.e., inside of the boundary layer [30–32]. In this study, 16 different rectangular integration contours with a distance d from the airfoil as a fraction of the chord length c varying between $d_{\min}/c = 0.1$ and $d_{\min}/c = 0.25$ in all four directions are used per spanwise section of the wing, as illustrated in Fig. 1. The results from the 16 different contours are averaged to reduce the influence of random measurement errors of the flow velocity field on the result for the lift.

In the case of moving wings in unsteady flow, the time-dependent lift per unit span $L'(t)$ can be divided into three contributions, following classic unsteady potential flow theory [33]: the lift due to bound circulation, the lift due to the shed circulation in the wake, and the noncirculatory lift (frequently called "added mass" lift). In the case of a relatively small degree of unsteadiness [reduced frequency of $k = (f\pi c)U_\infty^{-1} \ll 1$, with f being the frequency of the wing motion] and nonzero geometrical angles of attack α, the unsteady lift response will be dominated by the quasi-steady lift due to the time-dependent bound circulation $\Gamma_b(t)$, given by Eq. (1), where $\Gamma_b(t)$ is determined from the unsteady flowfield $\boldsymbol{u}(t)$ using Eq. (2). The additional unsteady lift contributions due to the shed circulation in the wake and the added mass can be determined using unsteady thin airfoil theory [34] so that the time-dependent lift is given as

$$L'(t) = \rho U_\infty \Gamma_b(t) + \rho \int_0^c \left(\frac{\partial}{\partial t} \Gamma_p(x, t) \right) \mathrm{d}x \tag{3}$$

The partial bound circulation as a function of the chordwise location $\Gamma_p(x, t)$ is obtained by performing line integrals of the measured flow velocity with integration contours that enclose the chord of the wing from the leading edge until the chordwise location x at which the partial circulation is evaluated, as described in Ref. [26].

B. Inertial Load

For the characterization of the dynamic aeroelastic interaction in response to the gust, only the dominant motion degree of freedom is considered, which is the deflection w of the wing in the direction perpendicular to the wing chord. A simplified one-dimensional model of the wing with a single coordinate z along the span is therefore considered for the inertial load determination, whereas the other motion degrees of freedom are not taken into account.

The inertial force per unit span I' on the wing can be determined as the product of mass density and acceleration:

$$I'(z, t) = -\mu(z)\ddot{w}(z, t) \tag{4}$$

where $\mu(z)$ is the mass per unit span of the wing section, and $\ddot{w}$ is the second temporal derivative of the out-of-plane wing deflection, which is calculated from the time series of reconstructed wing shapes using a second-order central finite difference scheme.

C. Elastic Load

The elastic force, as the third relevant aeroelastic force in a dynamic aeroelastic interaction, can be determined from the equilibrium of the three forces acting on the wing: $F_{\mathrm{elastic}} = -F_{\mathrm{aerodynamic}} - F_{\mathrm{inertial}}$. When the sectional aerodynamic and inertial forces have been determined along the span as described in the previous sections, these two forces can therefore be used to calculate the shear force distribution along the span of the wing. In this study, the elastic force is determined only in an integral sense at the root of the wing to perform a comparison of the nonintrusive measurements with force balance measurements. The force measurements that are obtained with a balance that is

attached to the root of the wing F_{root} correspond to the reaction force to the (elastic) shear force so that $F_{\mathrm{root}} = -F_{\mathrm{elastic}}$.

The dominant root force component in the wind-tunnel reference system is the root force in the y direction, which is determined by adding the y components of the aerodynamic and inertial loads and integrating the sum along the span:

$$F_{y,\mathrm{root}}(t) = \int_0^s (L'(z, t) + I'(z, t) \cos \alpha) \, \mathrm{d}z \tag{5}$$

The sectional lift force acts perpendicular to the direction of the freestream and is aligned with the y direction of the wind-tunnel reference system. The inertial force is determined according to Eq. (4) by considering the out-of-plane deflection in the reference system of the wing w. To obtain the integral force in the y direction, the contribution of the inertial load is therefore reduced by a factor of $\cos \alpha$, where α is the geometric angle of attack of the wing.

III. Experimental Setup and Procedures

A. Delft–Pazy Highly Flexible Wing Model

The Delft–Pazy wing is nearly identical to the benchmark Pazy wing described in detail in Ref. [9]. The wing has a nominal span of $s = 550$ mm, with a chord length of $c = 100$ mm and a NACA 0018 airfoil section. The wing is furthermore equipped with a 300-mm-long wingtip rod with a diameter of 10 mm (mass of about 15 g) that can be used to change the dynamic aeroelastic properties of the wing (see Ref. [9]). The wing structure consists of an aluminum spar and a three-dimensionally printed nylon chassis connected to a cylindrical mounting base. The assembly of the Delft–Pazy wing is performed analogously to the procedure described in Ref. [9]. The main difference from the benchmark Pazy wing design is the reduced thickness of the aluminum plate representing the spar of the Delft–Pazy wing, which is 1.5 mm as opposed to 2.25 mm for the original benchmark wing. The purpose of this design modification is to achieve similarly large deformations as observed in Ref. [9] at the reduced wind-tunnel speed, which was adjusted downward to facilitate the LPT measurements of the wing with the optical setup present in the wind-tunnel test section (see Sec. III.D). The mass of the wing including the wingtip rod but without the mounting base and connectors is estimated to be 279 g, based on the information given in Ref. [9] and considering the reduced plate thickness. The skin of the Delft–Pazy wing is made of Oralight black foil with a grid of white circular markers with diameters of 1.5 mm at the spanwise locations of the ribs and on the wingtip rod to perform the measurements of the structural response of the wing in the wind tunnel. The wing geometry and the fiducial marker grid specifications are shown in Fig. 2.
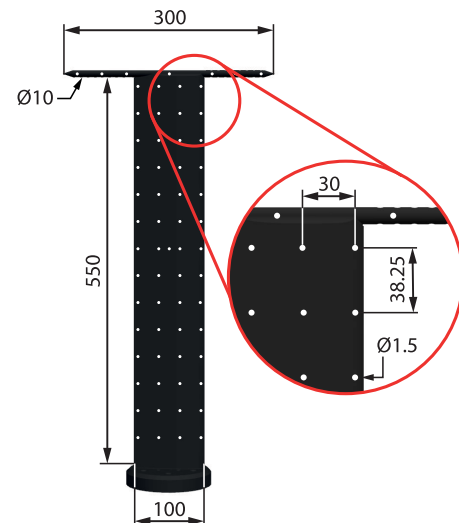

Fig. 2 Sketch of the dimensions (in millimeters) of the Delft–Pazy wing with detail of the fiducial marker grid.

The density of the marker pattern is insufficient to directly measure the wing deformation in terms of the local strain; instead, the purpose of the structural marker measurements is threefold; first, the marker measurements are used to transform the measurement coordinate system into wind-tunnel coordinates as described in Sec. IV.A. Second, they are used to determine the deformed wing shape according to the procedure described in Sec. IV.B, which is in turn used for the determination of the inertial force. Additionally, the marker-based wing shape reconstruction is used for selecting the circulation integration contours during the aerodynamic load determination based on the flowfield measurements.

B. Ground Vibration Test

A ground vibration test (GVT) and a finite element model simulation are used to characterize the structural dynamic behavior of the Delft–Pazy wing, in a similar approach as reported in Ref. [35]. The GVT measurements are conducted with a Polytec PSV-500 laser scanning vibrometer in a frequency range up to 800 Hz and postprocessed with the SimCenter TestLab software. An overview of the experimental setup of the GVT is shown in Fig. 3a. The vibration data are acquired at 37 different measurement points on the wing (see Fig. 3b), and the data from 10 measurements are averaged for each measurement point. The excitation of the wing model is achieved with a Maul-Theet vImpact-61 automatic modal hammer. The impact point of the modal hammer is near the leading edge of the wing at around one-quarter of the wingspan measured from the base, between the third and the fourth ribs, as is visible in Fig. 3b.

The results of the GVT in terms of the first five mode types, the modal frequencies, and damping are summarized in Table 1. The GVT results are correlated with a finite element model of the wing using the correlation tool in SimCenter 3D. The finite element model of the Delft–Pazy wing was derived from the finite element model of the original Pazy wing¶ by adjusting the spar thickness in the model to match the reduced plate thickness comprising the spar in the Delft–Pazy wing. The comparison between the GVT and the simulation results is shown in Fig. 4 and in Table 1. Figure 4 shows a qualitative comparison between the first five modes. The agreement between the mode shapes is very good, which is also indicated by very high values of the modal assurance criterion (MAC) [36] in Table 1. The agreement between the frequencies of the finite element model f_{FEM} and from the GVT f_{GVT} for the first five modes is very good, with an average difference of around 4% of the finite element model with respect to the GVT result, $\Delta f = (f_{FEM} - f_{GVT})/f_{GVT}$, which is similar to the agreement between the FEM and the GVT results reported in Ref. [9] for the original Pazy wing and in Ref. [35] for a similar wing design.

C. Wind-Tunnel Setup

The wind-tunnel experiments are conducted in the open-jet facility (OJF) at the Delft University of Technology. The OJF is an open test section closed-loop wind tunnel with an octagonal outlet that spans 2.85×2.85 m, which is operated at a freestream velocity of $U_\infty = 18.3$ m $\cdot$ s^{-1} during the experiments, corresponding to a Reynolds number of $Re = 122,000$ based on the wing chord. The Delft–Pazy wing model is mounted vertically in the test section on a force balance, which is attached to a rotating table that allows setting the geometric angle of attack α, defined with respect to the steady inflow direction. The balance and the rotating table are located underneath a splitter plate to reduce wind-tunnel interference effects. For the experiment, a gust generator is mounted at the wind-tunnel nozzle exit, which consists of two vertically mounted movable vanes that span the height of the wind-tunnel nozzle [37]. The wind-tunnel setup with an indication of the relevant components is shown in Fig. 5.

Four different test conditions are considered, of which two are with steady inflow conditions and two include the unsteady inflow produced by the gust generator. The conditions of the four test cases are
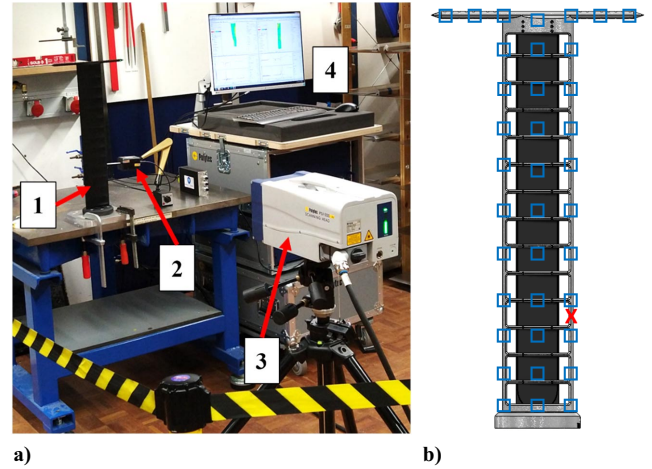
¶Available through the Third Aeroelastic Prediction Workshop https://nescacademy.nasa.gov/workshops/AePW3/public/wg/largedeflection.

Fig. 3 Representations of a) experimental setup for ground vibration test showing Delft–Pazy wing (no. 1), modal hammer (no. 2), laser scanning vibrometer (no. 3), and data acquisition computer (no. 4); and b) CAD model of wing without skin, with indication of GVT measurement points (blue squares) and driving point (red cross).

Table 1   Results of the ground vibration test and comparison with finite element model

Mode no.	Mode type	f_{GVT}, Hz	Damping rati, %o	f_{FEM}, Hz	Δf, %	MAC
1	First bending	3.2	0.54	3.3	+2.3	0.96
2	Second bending	22.5	0.60	21.9	−2.3	0.99
3	First torsion	29.5	0.61	28.1	−4.7	0.97
4	Third bending	65.0	0.60	63.1	−2.9	0.96
5	Second torsion	119.7	0.65	105.9	−11.5	0.73

summarized in Table 2. For the two test cases with steady inflow, the angles of attack are set to $\alpha = 5$ deg and $\alpha = 10$ deg, respectively, achieving different lift values, and thus different wing deformation levels. For the test cases with gust generator operation, the unsteady inflow is generated by a continuous sinusoidal operation of the gust generator during the measurement, with the gust vane angle described by $\beta = \beta_g \sin(2\pi f_g t)$, where β_g and f_g are the amplitude and frequency of the gust vane motion, respectively. Different frequencies are selected for the two dynamic test cases, corresponding to different levels of wing deformation and degrees of unsteadiness in the periodic inflow conditions. The first dynamic test case is selected to represent linear unsteady aerodynamic conditions because these conditions are relevant for applications in flight [2]. A moderate geometric angle of attack of $\alpha = 5$ deg is therefore selected, whereas the gust frequency is determined to be high enough to reach a reduced frequency of $k = f\pi U_\infty^{-1} = 0.1$, which is typically high enough to produce considerable unsteady aerodynamic effects [38]. The second dynamic test case is selected to study the gust response involving very large deformations. The angle of attack is therefore around the maximum value of the lift at $\alpha = 10$ deg to achieve a large mean deflection, and the wing is excited with a gust frequency that corresponds to the first natural bending frequency of the Delft–Pazy wing as it was measured in the GVT to produce large dynamic deflections around the mean deflection.

The gust vane amplitude is set to $\beta_g = 5$ deg in both test cases. Based on previous studies, it can be expected that this amplitude corresponds to a variation of the inflow angle to the wing with roughly half the amplitude of the gust vane motion: hence around 2.5 deg. Measurements of the gust inflow for the two considered dynamic test cases are shown in the Appendix. The variation of the inflow upstream of the wing is observed to be sinusoidal with an amplitude of 2.5 deg for the test case with $f_g = 5.7$ Hz and 2.0 deg for the test case with $f_g = 3.2$ Hz.
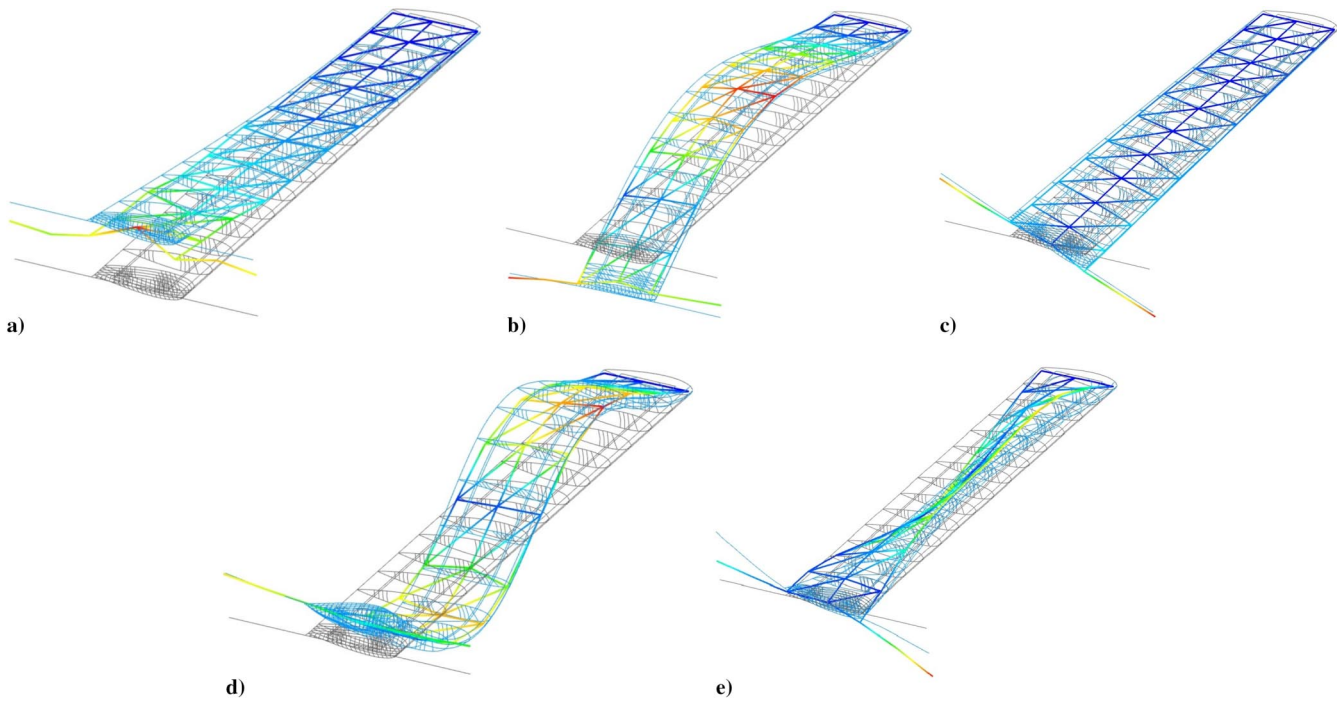
Fig. 4   Dynamic mode shape comparison between finite element model (light blue, with undeformed reference shape in gray) and GVT result (colored by displacement): a) first bending, b) second bending, c) first torsion, d) third bending, and e) second torsion.
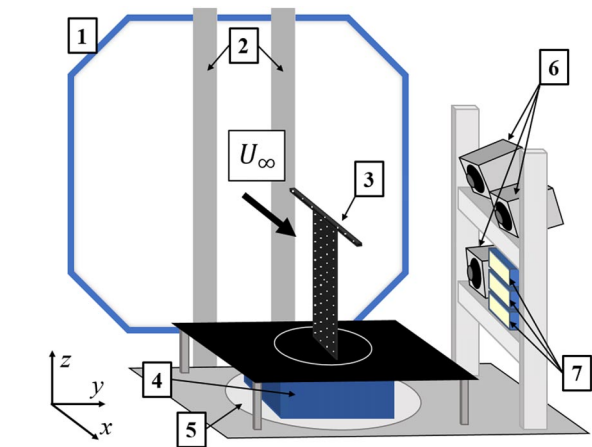

Fig. 5   Sketch of wind-tunnel setup in OJF: wind-tunnel outlet (no. 1), gust generator vanes (no. 2), Delft–Pazy wing (no. 3), force balance (no. 4), rotating table (no. 5), high-speed cameras (no. 6), and LED illumination units (no. 7).

Table 2   Summary of the wind-tunnel test conditions[a]

Test case	Wing geometric angle of attack α, deg	Gust vane amplitude β_g, deg	Gust frequency f_g, Hz	Reduced frequency k
1	5	N/A	N/A	0
2	5	5	5.7	0.10
3	10	N/A	N/A	0
4	10	5	3.2	0.055

[a]N/A denotes "not applicable."

D.   Lagrangian Particle Tracking System

For conducting the LPT measurements of the flow, the freestream is seeded with helium-filled soap bubbles (HFSBs) with diameters of about 0.5 mm that function as flow tracers [39]. The HFSB seeding generator, which consists of 200 bubble-generating nozzles covering an area of approximately 0.5 m in width and 1 m in height, is placed in the settling chamber of the OJF upstream of the wind-tunnel contraction to minimize the influence of the seeding generator on the freestream quality and to improve the seeding particle concentration in the test section. The working principle of the nozzles is described in Ref. [40]. The seeding particle concentration during the experiment was on the order of 1 cm^{-3}.

The optical measurement setup consists of three Photron Fastcam SA1.1 high-speed cameras with 50 mm lenses at a focal ratio of $f/22$. The cameras are operated at a recording frequency of 5.4 kHz with a resolution of 1024×1024 pixel (12-bit 20 μm pixel pitch). The illumination of the HFSB flow tracers and the fiducial markers on the wing is achieved with three LaVision light-emitting diode (LED)-flashlight 300 illumination units. The LPT data acquisition is performed with the LaVision Davis 10 software. An overview of the LPT measurement setup in the wind tunnel is shown in Fig. 6.

The size of the measurement volume that is obtained with this setup is about 300 mm in the x, y, and z directions, respectively. To achieve the complete aeroelastic characterization of the Delft–Pazy wing, which has a span width of 550 mm, measurements of the flowfield around the entire wing are necessary. Considering the measurement volume size and the limited optical access of the measurement setup, four separate measurements are performed for each test case. Each of the four measurements is covering roughly one-quarter of the entire investigated domain: one measurement volume is placed on the suction side and one on the pressure side for the upper and the lower halves of the wingspan, respectively. The adjustment of the spanwise position of the measurement volume is performed by changing the position of the cameras and illumination with respect to the wing. The measurements on the suction and pressure side of the wing are performed without moving the optical measurement setup and are instead made by changing the angle of attack of the wing to $+\alpha$ or $-\alpha$, respectively. For the test cases with steady inflow, the four acquisitions from the four different measurement volumes are combined into an integrated time-averaged representation during the LPT data postprocessing. For the dynamic test cases, five recordings, each with a duration of 1.01 s (5457 images per recording, corresponding to the full RAM size of the cameras), are performed for each of the four measurement volumes. These separate measurements are then combined into a phase-averaged representation of the flowfield during the postprocessing, which is necessary to improve the measurement resolution when considering the limited HFSB particle concentration.
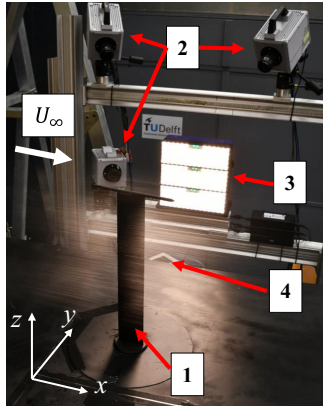
Fig. 6 Photograph of Lagrangian particle tracking measurement setup in wind tunnel: Delft–Pazy wing (no. 1), high-speed cameras (no. 2), LED illumination units (no. 3), and stream of illuminated helium-filled soap bubbles (no. 4).

IV. Integrated Measurement Approach

The measurement data processing steps that are applied to analyze the static and dynamic aeroelastic behaviors of the Delft–Pazy wing are visualized in Fig. 7. The data processing of the integrated optical measurements to obtain separate LPT measurements of the flow and the structure is described in Sec. IV.A. The further postprocessing of these measurements to obtain the wing shape reconstruction and the ensemble-averaged volumetric flowfields are described in Secs. IV.B and IV.C, respectively. Section IV.C also contains an analysis of the unsteady flowfields with respect to the effective inflow angles to the wing. The results for the wing shapes and the flowfields are analyzed afterward, as described in Secs. II.A and II.B, to achieve the characterization of the aeroelastic loads acting on the wing. To validate these results, a comparison is made to force balance measurements in terms of the root force on the wing, as described in Sec. II.C. The processing of the force balance measurements is described in Sec. IV.D.

A. Optical Measurements Data Processing

The processing of the integrated optical measurements is performed with the LaVision Davis 10 software and begins with the geometrical calibration of the measurement system and a volume self-calibration [41]. Subsequently, the flow tracers are separated from the structural markers in the acquired images so that a nonuniform optical transfer

function [42] can be generated for the structural markers and the flow tracers separately. The removal of the structural information from the integrated measurement images is achieved with a temporal high-pass filter [43], exploiting the different timescales between the flow and the structural motion. The reverse operation is applied to obtain the image data of the structural markers without the flow tracer information by using a temporal low-pass filter [44]. This image separation procedure is illustrated in Fig. 8.

After separating the flow and structural information and completing the optical calibration, the next step is to perform the LPT analysis, for which the shake-the-box algorithm is used [25]. The results are obtained in terms of individual Lagrangian particle tracks (with the position, velocity, and acceleration of each particle over time) for both the structural markers and the flow tracers in separate datasets. These measurements are postprocessed in a time- or phase-averaged sense for the test cases with steady and unsteady periodic inflows, respectively.

A further necessary postprocessing step of the LPT data is the transformation of the measurement coordinate system to the wind-tunnel coordinate system. This is achieved by acquiring a reference measurement of the structural markers on the Delft–Pazy wing without wind-tunnel operation after each adjustment of the measurement volume. These data are then correlated with the reference positions of the markers painted on the model to determine the translations and rotations of the measurement coordinates with respect to the wind-tunnel coordinates, which are then used to transform the LPT measurements into the wind-tunnel coordinate system. The accuracy of the employed merging procedure can be assessed by comparing the measured flow velocity at corresponding positions with respect to the wing from different acquisitions. Typical values of these differences are between 1 and 3% of the local velocity magnitude. Because these values are of the same order of magnitude as when the merging of different flow measurement acquisitions is performed automatically based on position measurements with a robotic arm [45], these differences are considered acceptable and not further investigated.

B. Wing Shape Reconstruction

After the LPT measurements of the fiducial markers on the wing are transformed into the wind-tunnel coordinate system, the position measurements of the markers are used to determine the deformed shape of the wing. This is achieved by calculating an average local deflection $w(z)$ for each spanwise section where the markers were painted (i.e., the ribs of the wing) from the measurements and then fitting a polynomial curve through these measurements along the
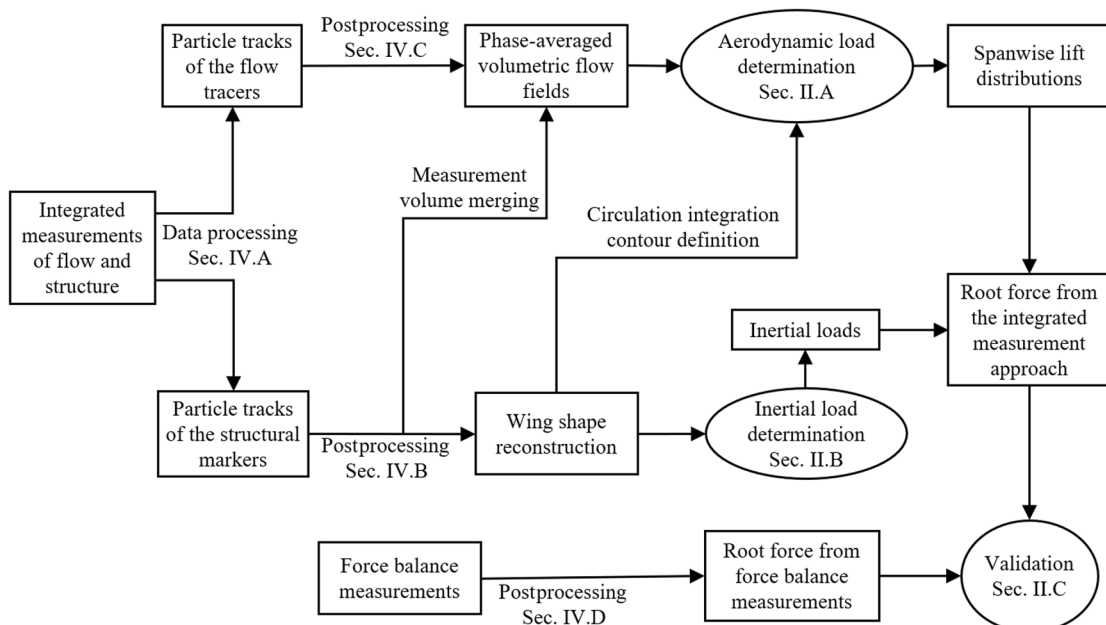

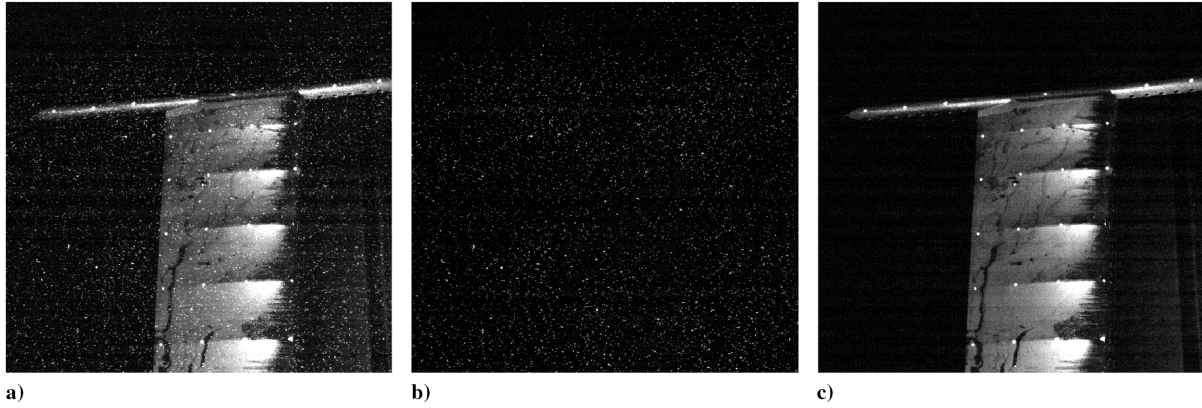**Fig. 7 Flowchart of the data processing steps applied in this study.**

Fig. 8 Image data processing: a) integrated optical measurement of flow and structure, b) image data of the flow tracers, and c) image data of the structure.

spanwise direction. Following this procedure, the polynomial curve fit can be used as a reference spanwise axis to calculate the deformed wing shape. A fourth-order polynomial is used for the curve fit, which satisfies the geometric boundary conditions of the wing that is clamped at the root, $w(z = 0) = 0$ and $\partial w/\partial z(z = 0) = 0$, and is defined as

$$w(z) = Az^4 + Bz^3 + Cz^2 \quad (6)$$

where the coefficients A, B, and C are optimized to provide the best fit to the experimental wing shape measurements in a least-squares sense. The results of the polynomial curve fit to the measurements for the two test cases with steady inflow are shown in Fig. 9. The length of the polynomial curve is adjusted to match the undeformed shape by numerically integrating the length of the polynomial curve to determine the value of z_{tip} in the deformed case that corresponds to an arc length that is equal to the span s of the undeformed wing.

The measurements of the marker positions that are shown in Fig. 9 are averaged from 1000 images acquired in the wind tunnel to reduce the effect of measurement noise and small-scale vibrations of the wing during the experiment. Furthermore, the deflection measurements obtained from the eight markers that are distributed along the chord on both sides of the wing are averaged to produce only one measurement data point per spanwise location. With this approach, the standard deviation of the residual between the 15 measurement data points along the span and the curve fit is $\sigma = 0.13$ mm for $\alpha = 5$ deg and $\sigma = 0.25$ mm for $\alpha = 10$ deg, corresponding to less than 0.5% of the respective wingtip displacement. To fully describe the deformed wing shape, the torsional deformation in terms of a twist angle ϵ of the wing around the reference axis is required as well. The twist angle can be estimated from the marker measurements with the average displacements of the marker measurements near the leading edge (LE) and the trailing edge (TE) as

$$\epsilon(z) = \arctan\left(\frac{y_{TE}(z) - y_{LE}(z)}{x_{TE}(z) - x_{LE}(z)}\right) \quad (7)$$

The experimental wingtip twist angles that are found using Eq. (7) are below $\epsilon_{tip} < 0.4$ deg for both α. Even though the magnitude of

these values for the twist is not necessarily negligible in an aerodynamic sense, these values are considered negligible for the wing shape reconstruction because the twist angle of the wing is of no direct interest for the experimental load determination that is performed in this study. Employing this assumption simplifies further analysis and avoids the influence of random measurement errors of the wing twist along the span on the wing shape reconstruction.

To reconstruct the dynamic response of the wing to the periodic unsteady inflow, the marker measurements obtained in these cases are processed in a similar way as for the steady inflow but now analyzed in a phase-averaged sense, which means that measurements from different periods are collected at the respective time expressed as a fraction of the period: t/T. To reduce the effect of random measurement noise and outliers that may result from light reflections in some of the acquired images, a temporal smoothing procedure using a sinusoidal curve fit is applied. The wing is expected to oscillate around the static deflected shape, and the temporal smoothing is therefore performed after transforming the marker measurements per wing section into the reference system of the static deflected wing shape at the respective angle of attack. The displacement measurements in their local coordinate system and the corresponding sinusoidal fits are shown for two spanwise locations for both dynamic test cases in Figs. 10 and 11, respectively. For reference, the measured gust inflow (see the Appendix) is indicated in the figures as well.

With this approach, the sinusoidal curve fit provides a good approximation of the temporal behavior, with a standard deviation of the residual of the sinusoidal fit around $\sigma = 0.1$ mm for the $f_g = 5.7$ Hz gust at $\alpha = 5$ deg and $\sigma = 0.2$ mm for the $f_g = 3.2$ Hz gust at $\alpha = 10$ deg. The twist angle of the wing varies withing the range of 0 deg $< \epsilon < 0.5$ deg in the first case and 0 deg $< \epsilon < 1$ deg in the second case, which is, as in the cases with steady inflow, considered sufficiently small to be neglected for the purpose of this study. After the phase-averaged marker measurements per spanwise location are determined based on the respective sinusoidal fits, the smoothed measurements are transformed back into the wind-tunnel coordinate system; afterward, the same polynomial curve fitting procedure as in the steady cases is applied for each phase instant of the dynamic response. The time series of the fitting coefficients obtained with this procedure allows the reconstruction of a smooth deformed wing
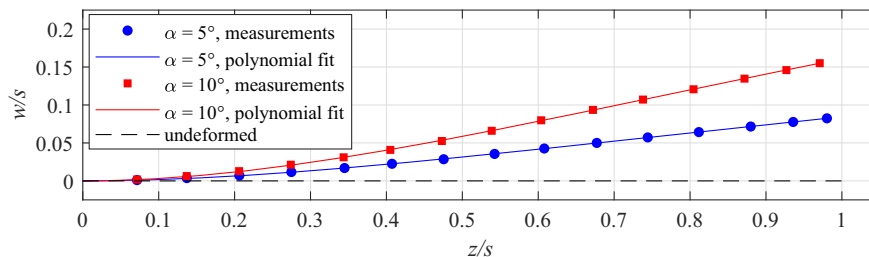

Fig. 9 Deflection measurements in steady inflow with polynomial curve fit.
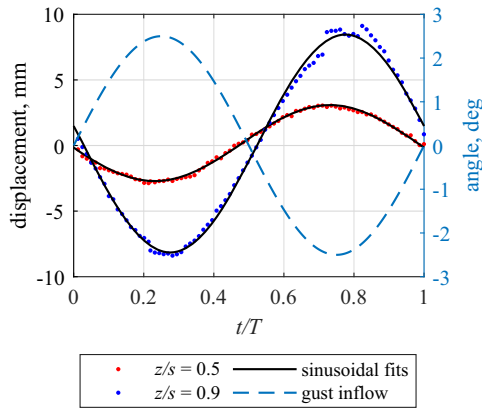
Fig. 10 Measurements of the dynamic displacement with sinusoidal fits at two spanwise locations of the wing at $\alpha = 5$ deg for the gust with $f_g = 5.7$ Hz.
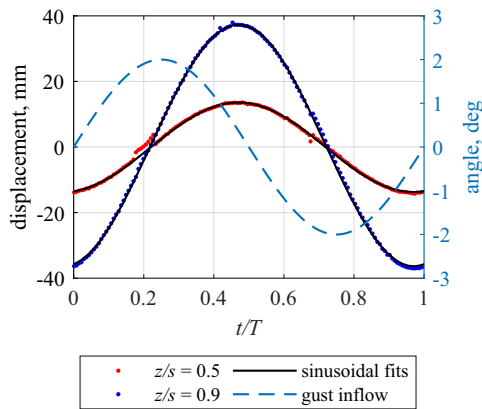

Fig. 11 Measurements of the dynamic displacement with sinusoidal fits at two spanwise locations of the wing at $\alpha = 10$ deg for the gust with $f_g = 3.2$ Hz.

shape variation over the entire period, yielding the phase-averaged behavior of the wing deformation in response to the gust. As an illustration, the reconstructed wing shapes at the phase instants with the minimum and maximum deflections are shown in Figs. 12 and 13 for the two dynamic test cases. The wing shape reconstructions are used to compute the inertial loads acting on the wing along the span, to define the circulation integration contours for the lift determination from the flowfield, and in the following for characterizing the dynamic wing response to the gust forcing.

The main features of the structural response of the wing to steady and unsteady inflow conditions, as determined based on the wing shape reconstructions, are summarized in Table 3. As expected, the higher geometric angle of attack produces larger deflections in steady inflow, with the wingtip deflection scaling nearly linearly with the angle of attack. On the other hand, the dynamic response to the two gusts is different in terms of both the deflection amplitude as well as the phase shift Φ that is calculated with respect to the gust arriving at the wing, despite the identical gust forcing amplitudes. These differences can be attributed to the different forcing frequencies of the gust with respect to the frequencies of the dynamic modes of the Delft–Pazy wing that were identified in the GVT (see Table 1). The first gust frequency of $f_g = 5.7$ Hz is well above the first bending frequency of the wing but clearly below the second bending and first torsion modal frequencies. As a result, the dynamic response of the wing is relatively small in amplitude, with a phase shift of nearly $\Phi \approx \pi$ with respect to the gust forcing. For the second gust case, the gust frequency is identical to the frequency of the first bending mode: $f_g = 3.2$ Hz. In this case, the dynamic response is observed to be much larger in amplitude and shifted in phase by around $\Phi \approx 0.5\pi$. Overall, these observations are in close correspondence to the theoretical frequency response of a harmonically forced system [46].
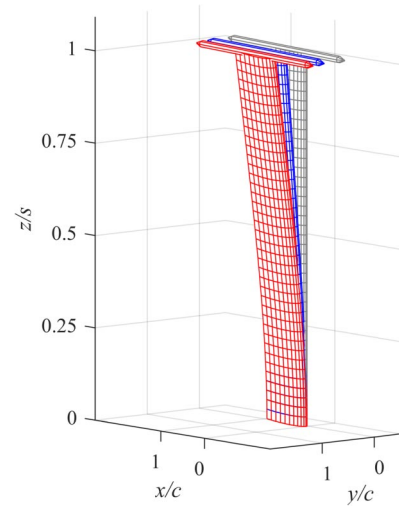

Fig. 12 Wing shape reconstructions for the wing at $\alpha = 5$ deg and the gust with $f_g = 5.7$ Hz: maximum deflection (red), minimum deflection (blue), and undeformed reference (gray).
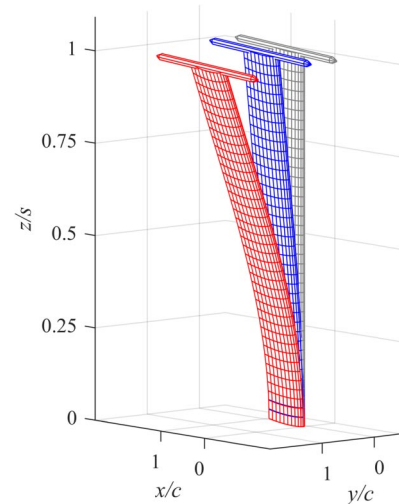

Fig. 13 Wing shape reconstructions for the wing at $\alpha = 10$ deg and the gust with $f_g = 3.2$ Hz: maximum deflection (red), minimum deflection (blue), and undeformed reference (gray).

C. Flowfield Processing and Analysis

The particle tracks of the flow tracers obtained from the LPT analysis provide the time series of a large number of discrete measurements of the flow velocity, which are obtained in the measurement coordinates of the LPT system. These measurements are transformed into the coordinate system of the wind tunnel as described in Sec. IV.A. Subsequently, the measurements are ensemble averaged onto a Cartesian grid, as described in Ref. [47]. A Cartesian grid with a grid spacing of 3.75 mm is used, and an overlap of 75% is applied in the ensemble averaging. The three-dimensional flowfield that results from this procedure is visualized in Figs. 14 and 15 for the test cases with steady inflow at $\alpha = 5$ deg and $\alpha = 10$ deg, respectively. The plots show the marker-based reconstruction of the deformed wing shape together with the ensemble-averaged flowfield, which is visualized in five slices along the span and with two isosurfaces of the streamwise velocity.

It is evident in the flow visualizations that the increase in the angle of attack from $\alpha = 5$ deg to $\alpha = 10$ deg corresponds to enlarged areas of accelerated flow on the suction side (indicated by the red isosurface) and decelerated flow near the stagnation point on the pressure side of the wing (indicated by the blue isosurface). Furthermore, the formation of a region of decelerated flow near the trailing edge on the suction side of the wing is visible in Fig. 15, which is a result of the boundary layer that forms on the wing and increases in

Table 3   Summary of the structural response of the wing to steady and unsteady inflows

Geometric angle of attack	Static tip deflection	Gust frequency	Dynamic tip deflection amplitude	Phase shift to gust inflow
$\alpha = 5$ deg	$w_{\text{tip}}/s = 8.5\%$	$f_g = 5.7$ Hz	$\hat{w}_{\text{tip}}/s = 1.8\%$	$\Phi = -0.95\pi$
$\alpha = 10$ deg	$w_{\text{tip}}/s = 15.9\%$	$f_g = 3.2$ Hz	$\hat{w}_{\text{tip}}/s = 8.2\%$	$\Phi = 0.55\pi$
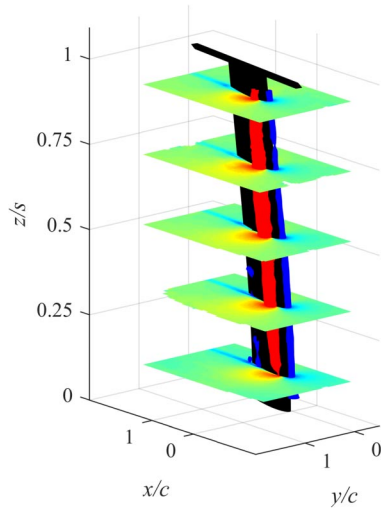
Fig. 14   Wing shape reconstruction at $\alpha = 5$ deg, with five slices of the streamwise velocity field and isosurfaces of the streamwise velocity (blue: $0.75U_\infty$, red: $1.25U_\infty$).
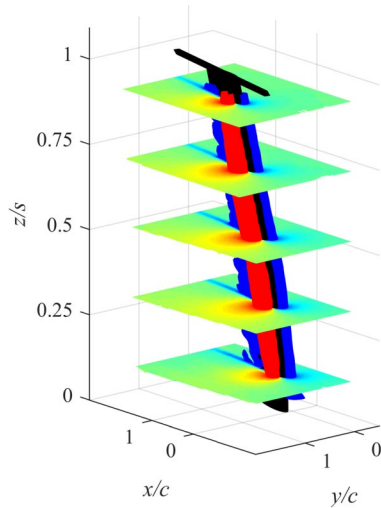
Fig. 15   Wing shape reconstruction at $\alpha = 10$ deg, with five slices of the streamwise velocity field and isosurfaces of the streamwise velocity (blue: $0.75U_\infty$, red: $1.25U_\infty$).

thickness with increasing α, thus having a stronger effect on the flowfield at $\alpha = 10$ deg than at $\alpha = 5$ deg. The flowfields for both angles of attack exhibit little spanwise variation, except for the regions in the vicinity of the wing root and wingtip, which could not be fully captured due to the size limitations of the LPT measurement volumes.

For the test cases with unsteady periodic inflow, the particle tracks from the LPT analysis are assigned a phase value t/T to postprocess the flowfields in a phase-averaged manner. The ensemble averaging is therefore performed for 25 temporal bins distributed over the period, with each spanning a fraction of 4% of the respective period T. For each subset of the LPT data that is collected in one temporal bin, the ensemble averaging is performed in the same way as for the test cases with steady inflow. The results of the flow data postprocessing for the test cases with unsteady inflow are visualized in Fig. 16 for $\alpha = 5$ deg and in Fig. 17 for $\alpha = 10$ deg, where the

phase-averaged flowfield is shown together with the reconstructed wing section for four different phase instants at mid-span.

The four plots in Fig. 16 show no appreciable variation of the location of the wing section over the period, but the flowfields exhibit a notable variation over the gust cycle, where the regions of accelerated and decelerated flows are enlarged at $t/T = 0.25$ and reduced at $t/T = 0.75$ when compared to the flowfields at $t/T = 0$ and $t/T = 0.5$, which appear as similar. These effects can be directly linked to the sinusoidal gust inflow and explained with linear aerodynamics theory. The observations for the flowfields shown in Fig. 17 are different; whereas the location of the wing section varies more than in Fig. 16 due to the different gust frequency, the flowfields, in this case, remain nearly unchanged over the period. The explanation for this difference between the aerodynamic response of the wing to the two gusts is twofold. First, the geometric angle of attack of $\alpha = 10$ deg for the second gust is outside of the linear lift regime, whereas the flow on the wing is still mostly attached. This means that at this particular angle of attack, the lift is less sensitive to changes in α, and changes in the inflow angle do not translate directly into enlarged regions of acceleration and deceleration around the wing. Second, the influence of the wing motion on the effective inflow angle α_e that is experienced by the wing differs between the two gusts, due to the differences in amplitude and phase of the structural response. The effective inflow angle is calculated as

$$\alpha_e(z,t) = \alpha + \alpha_g(t) + \alpha_v(z,t) \tag{8}$$

where α is the geometric angle of attack of the wing, α_g is the inflow angle of the gust, and α_v is the inflow angle induced by the motion of the wing:

$$\alpha_v(z,t) = -\arctan\left(\frac{v_{\text{wing}}(z,t)}{U_\infty}\right) \tag{9}$$

The different contributions to the effective inflow angles are shown in Figs. 18 and 19 for the two dynamic test cases, respectively. The geometric angle α is constant, whereas the gust inflow angle α_g varies sinusoidally, as determined based on the measurements of the gust inflow (see the Appendix). The inflow angles induced by the wing motion α_v are calculated from the transversal velocity v_{wing} of the reconstructed wing shapes at three different spanwise locations. The results for the effective inflow angles over the period for these three locations are shown in Figs. 20 and 21.

In Fig. 20, it is visible that all curves are similar, implying that the influence of the wing motion on the inflow angle for the gust with $f_g = 5.7$ Hz is relatively small. The effects of the wing motion are a lag in the effective inflow with respect to the gust inflow ($|\Delta t/T| < 0.1$) and an increase in amplitude ($|\Delta \alpha_e| < 0.5$ deg) of the inflow angle toward the wingtip. For the gust with $f_g = 3.2$ Hz, the effect of the wing motion on α_e is substantially larger, as is visible in Fig. 21. In this case, the inflow angle induced by the wing motion α_v is in antiphase with the gust inflow and large enough in amplitude to considerably reduce the variation in α_e and to invert the phase angle of the variation of α_e toward the wingtip. These differences in the behavior of the effective inflow angle between the two gusts are in direct correspondence to the different aerodynamic behavior shown in Figs. 16 and 17. The implications of this behavior for the unsteady lift force are discussed in Sec. V.B.

D.   Balance Data Processing

The balance data were acquired at a sampling rate of 100 Hz simultaneously with the optical measurements, which means that there are four measurements for each test case with steady inflow,
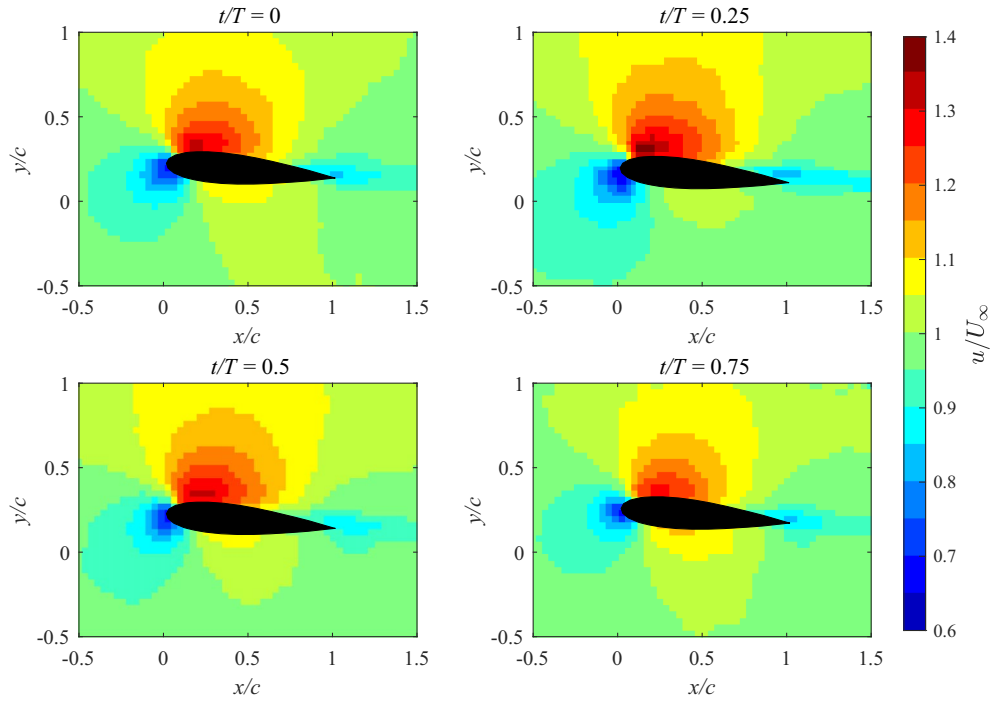
Fig. 16 Ensemble-averaged streamwise velocity at $z/s = 0.5$ in four different phase instants at $\alpha = 5$ deg for the gust with $f_g = 5.7$ Hz.
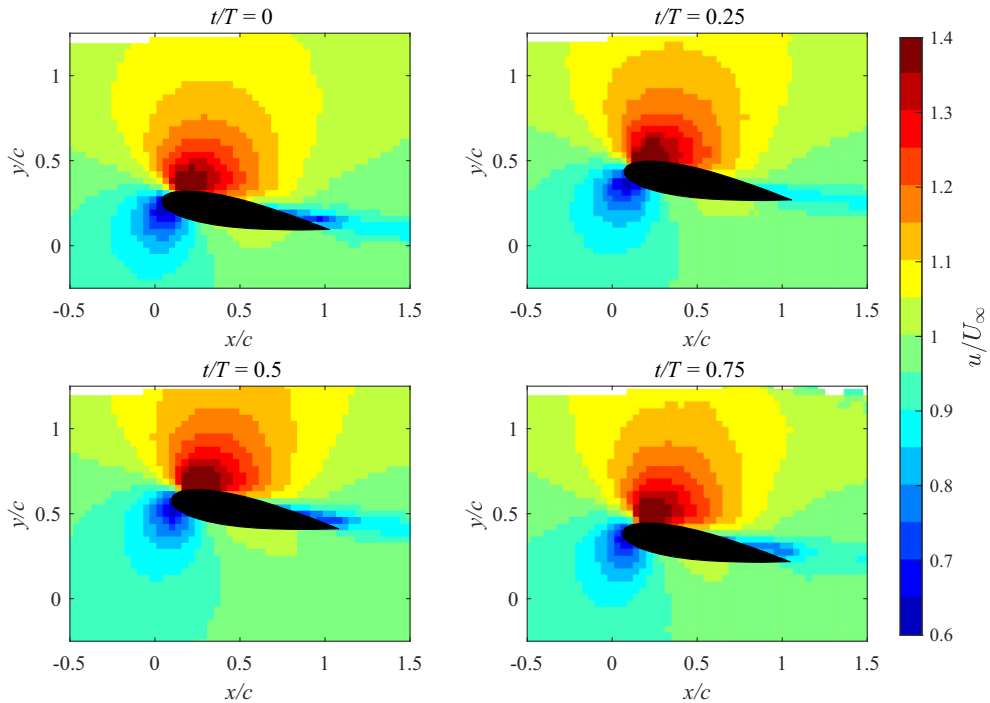

Fig. 17 Ensemble-averaged streamwise velocity at $z/s = 0.5$ in four different phase instants at $\alpha = 10$ deg for the gust with $f_g = 3.2$ Hz.

corresponding to the four different measurement volumes, and 20 separate measurements for each of the test cases with dynamic inflow (five acquisitions for each of the four measurement volumes). For the test cases with steady inflow, the balance measurements of the root force in the y direction from the different acquisitions are first averaged in time, and then the mean and standard deviation of the four acquisitions are calculated to be used as a reference for the nonintrusive loads.

For the dynamic test cases, the balance measurements are phase averaged using 25 temporal bins, which is analogous to the phase-averaging procedure applied for the LPT data. The results from the phase averaging of the root force measured with the balance are

shown for both test cases in Fig. 22. The mean and the standard deviation of all 20 phase-averaged measurements are depicted as solid lines with error bars, whereas the individual measurements are plotted in shaded colors, corresponding to the respective test case.

The root force measurements with the balance show little variation over the period for the dynamic inflow with $f = 5.7$ Hz at $\alpha = 5$ deg. For the dynamic inflow with $f = 3.2$ Hz at $\alpha = 10$ deg, the force shows a cosine-shaped variation over the period. Despite the phase averaging that is applied to the individual measurements, the balance measurements still show a considerable variation between different acquisitions for the same test condition, with standard deviations of the root force around 0.6N in both test cases.
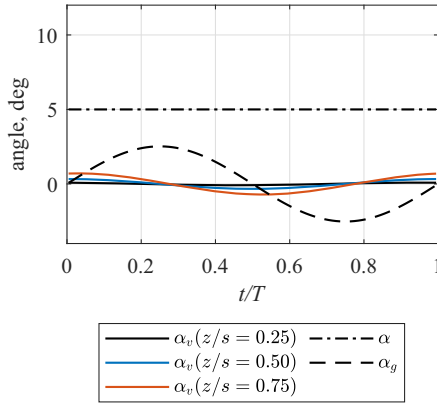
Fig. 18 Separate contributions to the effective inflow angle for the gust with $f_g = 5.7$ Hz at $\alpha = 5$ deg.
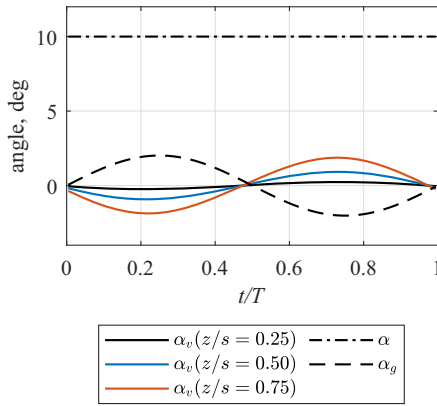

Fig. 19 Separate contributions to the effective inflow angle for the gust with $f_g = 3.2$ Hz at $\alpha = 10$ deg.
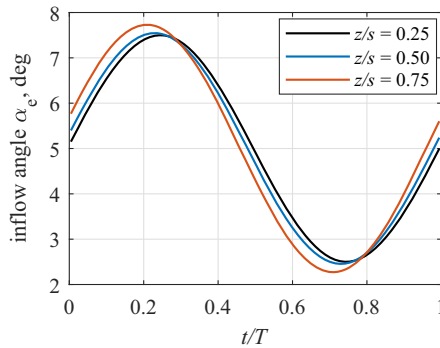

Fig. 20 Effective inflow angles at different spanwise locations for the gust with $f_g = 5.7$ Hz at $\alpha = 5$ deg.
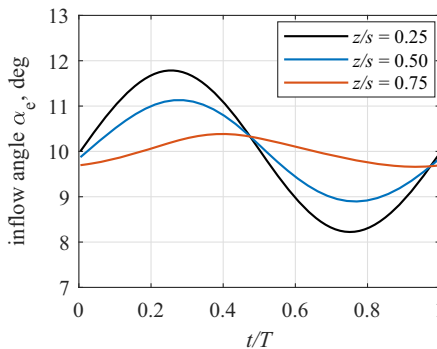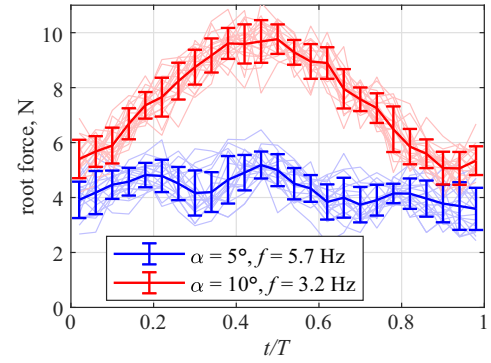

Fig. 21 Effective inflow angles at different spanwise locations for the gust with $f_g = 3.2$ Hz at $\alpha = 10$ deg.

Fig. 22 Phase-averaged root force in the y direction measured with the balance for both dynamic test cases.

V. Results

A. Static Aeroelastic Characterization

The lift per unit span L' is determined from the time-averaged flowfield measurements using Eqs. (1) and (2). To illustrate the sensitivity of the lift to the position of the integration contour, Fig. 23 compares the sectional lift in terms of the lift coefficient, $C_\ell = L' ((1/2)\rho U_\infty^2 c)^{-1}$, as determined when using different contours for the integration of the circulation for $\alpha = 5$ deg at $z/s = 0.5$. The 25 different integration contours that are considered were obtained by independently varying the distances d from the airfoil surface (see Fig. 1) in five steps from $0.1c$ to $0.3c$ in the x and y direction s, respectively. Overall, the variation of C_ℓ as a function of the circulation integration contour is small, with a standard deviation of $\sigma = 0.002$, corresponding to 0.5% of the lift coefficient in this case. The only consistent trend that is visible is a small increase of the lift for the largest contour in the y direction. Because there is no physical explanation for this variation of the lift, this effect is likely to be caused by systematic measurement errors toward the edge of the measurement volume. Hence, the reference lift $C_{\ell,\mathrm{ref}}$ is computed as the average of the 16 integration contours in the range $0.1 < d/c < 0.25$.

To further analyze the sensitivity of the lift to the properties of the experimental data, the effect of the particle concentration and the number of circulation integration contours used for averaging on the result for the lift coefficient is shown in Fig. 24. The particle concentration is varied by deleting particles from the original distribution, which has a concentration of 1278 cm^{-3} for the investigated section of the dataset. The effect of averaging multiple integration contours is shown by using an increasing number of contours N between one and 16 for the averaging, which are selected at random from the range $0.1c < d < 0.25c$. The result is quantified in terms of the lift residual δ, which is defined with respect to the reference lift coefficient:

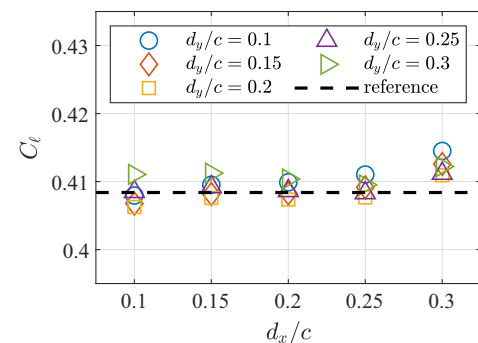$$\delta = \frac{|C_\ell - C_{\ell,\mathrm{ref}}|}{C_{\ell,\mathrm{ref}}} \tag{10}$$

Fig. 23 Lift coefficient for different circulation integration contours: $\alpha = 5$ deg at $z/s = 0.5$.
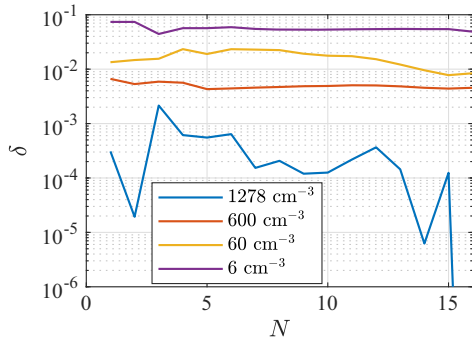
Fig. 24 Lift residual over the number of circulation integration contours used for averaging with various particle concentrations: $\alpha = 5$ deg at $z/s = 0.5$.

The residual generally decreases with increasing particle concentration and N; however, a consistent trend is observed mainly for the particle concentration, where the residual decreases by several orders of magnitude with an increasing number of particles. On the other hand, the difference between the lift result that is obtained using the largest amount of data (16 integration contours with a particle concentration of 1278 cm^{-3}), which is $C_{\ell,\text{ref}} = 0.408$, and the lift result from a much smaller amount of data (one integration contour with a particle concentration of 60 cm^{-3}), which is $C_\ell = 0.414$, is relatively small at around 1.4%.

Following the sensitivity analysis of the sectional lift to the position of the integration contour, the sectional lift is determined as the average of the 16 circulation integration contours with the distances to the wing varying between $d_{\min}/c = 0.1$ and $d_{\max}/c = 0.25$ in all four directions, using all available particle data. This procedure is applied along the entire span. To obtain a smooth spanwise lift distribution, the results from all contours are averaged over a range of 5% of the span. The lift distributions for both α using this approach are shown in Fig. 25. As expected, the lift is generally higher for $\alpha = 10$ deg, but the two lift distributions are qualitatively similar. Both lift curves show a gradual drop of lift toward the tip, as is expected from aerodynamics theory [29]. A small drop of lift toward the root is visible for $\alpha = 5$ deg that can be associated with the presence of a boundary layer on the table on which the wing is mounted. The drop of lift toward the root is more pronounced for $\alpha = 10$ deg, which is likely caused by the strong deformations of the wing section shape near the root as the wing is bending, providing a less effective aerodynamic shape in this region of the wing.

To perform a quantitative assessment of the results for the lift, the lift distributions for both α values are integrated along the span and compared to the measurements of the force at the root with the balance. The results of this comparison are shown in Table 4. The agreement of the root force values measured nonintrusively and with the balance is very good, with differences at around 1% of the root force. These differences are in the same order of magnitude as the standard deviation of the balance measurements from different measurement acquisitions.
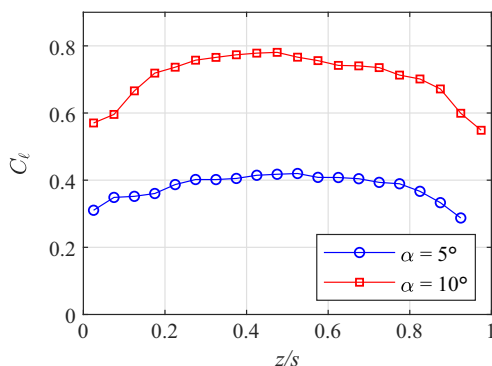
Table 4 Comparison of the root shear force measured with the integrated approach and the balance in steady inflow conditions

Geometric angle of attack	Root shear force (nonintrusive)	Root shear force (balance)	Relative difference $\Delta F_y/F_{y,b}$
$\alpha = 5$ deg	$F_y = 4.14$ N	$F_{y,B} = 4.12$ N $\pm$ 0.17 N	+0.6%
$\alpha = 10$ deg	$F_y = 7.77$ N	$F_{y,B} = 7.64$ N $\pm$ 0.10 N	+1.7%

B. Dynamic Aeroelastic Characterization

For the test cases with dynamic inflow, the aerodynamic loads are determined with Eq. (3), using additional circulation integration contours to obtain the partial circulation along the chord. Apart from the inclusion of the additional unsteady term, the calculations of the lift distributions along the span for each phase instant of the dynamic cases follow the same procedure as in the static cases. The results for the lift distributions at four phase instants are shown for both dynamic test cases in Figs. 26 and 27, respectively. The standard deviations of the lift variation due to the choice of the integration contour have been assessed to be not significant, having typical values of less than 1% of the lift for both dynamic test cases.

As visible in Fig. 26, the four lift distributions along the span for the different phase instants are qualitatively similar for $\alpha = 5$ deg and $f_g = 5.7$ Hz but vary in lift magnitude. From the four phase instants that are shown, the highest lift occurs at $t/T = 0.25$ over the entire span width. In contrast, the spanwise lift distributions for $\alpha = 10$ deg and $f_g = 3.2$ Hz in Fig. 27 do not vary strongly in magnitude but exhibit a qualitatively different behavior, depending on the phase instant. It is visible that for $t/T = 0.25$, the maximum lift over the span occurs relatively close to the root at around $z/s = 0.3$; whereas for $t/T = 0.75$, the spanwise maximum of the lift is around $z/s = 0.75$.
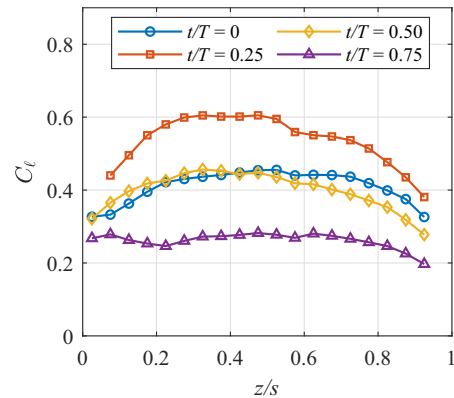

Fig. 26 Spanwise lift distributions at $\alpha = 5$ deg for the gust with $f_g = 5.7$ Hz.

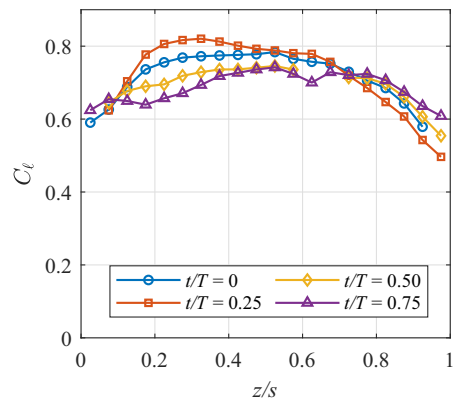**Fig. 25 Spanwise lift distributions for the test cases with steady inflow.**

Fig. 27 Spanwise lift distributions at $\alpha = 10$ deg for the gust with $f_g = 3.2$ Hz.

Further analysis of the unsteady lift behavior is provided in Figs. 28 and 29, where the temporal behavior of the lift is shown for three spanwise locations of the wing for both dynamic test cases, respectively. Following the behavior of the spanwise lift distributions and the analysis of the effective inflow angles in Sec. IV.C, the temporal behavior of the lift for $\alpha = 5$ deg and $f_g = 5.7$ Hz is sinusoidal for each spanwise location. The effect of the unsteady lift terms on the temporal behavior of the lift is indicated in the plots as well. In this test case, the unsteady lift contribution due to the circulation in the wake is noticeable and causes a lag of the lift with respect to the quasi-steady lift due to the bound circulation. For the test case with $\alpha = 10$ deg and $f_g = 3.2$ Hz that is shown in Fig. 29, the temporal behavior of the lift is clearly sinusoidal only near the root and shows less temporal variation for the outer part of the wing, which is in agreement with the analysis of the effective inflow angles (see Fig. 21). In this case, the lift variation is smaller than in the other test case and further decreased as compared to the analysis of the effective inflow angles due to the nonlinear lift behavior that occurs for the range of α_e of this test case. Furthermore, the gust frequency is lower, which leads to an overall decreased significance of the unsteady lift contributions: in particular, for the outer part of the wing.

For performing the comparison between the nonintrusive load measurements and the root force measured with the force balance, the lift distributions for both dynamic test cases are integrated along the span. The temporal variation of the spanwise-integrated lift force is shown for both test cases in Fig. 30. The variation of the lift is considerably larger for the gust with $f_g = 5.7$ Hz at $\alpha = 5$ deg, with a peak-to-peak amplitude of almost 3 N, as compared to less than 1 N for the gust with $f_g = 3.2$ Hz at $\alpha = 10$ deg. The analysis of the separate contributions of the unsteady and quasi-steady terms to the lift reveals that the unsteady terms cause a phase lag of the lift for the gust with $f_g = 5.7$ Hz of $\Delta t/T = 0.029$, as compared to the quasi-steady lift. For the gust with $f_g = 3.2$ Hz, the contribution of the unsteady terms to the overall lift is always below 0.1 N, and thus negligible.

The inertial loads as determined from the time series of the reconstructed wing shapes and Eq. (4) as described in Sec. II.B are
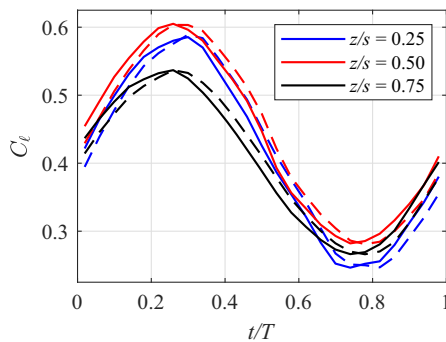
shown in Figs. 31 and 32 for the two dynamic test cases, respectively. The plots show the variation of the sectional inertial force over the period at three spanwise locations. The temporal behavior of the inertial load is qualitatively identical along the span, with the load magnitude increasing with the spanwise coordinate.

As for the aerodynamic load, the inertial load is integrated along the span to validate the nonintrusive measurements with the force balance, as shown in Fig. 33 for both dynamic test cases. The magnitudes of the inertial force are similar for both test cases. When compared to the aerodynamic force, the amplitudes of the inertial force are significant: for the gust with $f_g = 5.7$ Hz the amplitude of the inertial force is around 37% of the temporal mean of the aerodynamic force; and for the gust with $f_g = 3.2$ Hz, the inertial force amplitude is 29% of the aerodynamic force. The phase difference between the inertial force of the two cases is around one-quarter of the

Fig. 30 Root force over the period resulting from the aerodynamic load for both dynamic test cases.

Fig. 28 Unsteady lift (solid lines) and quasi-steady lift (dashed lines) over the period at $\alpha = 5$ deg for the gust with $f_g = 5.7$ Hz.
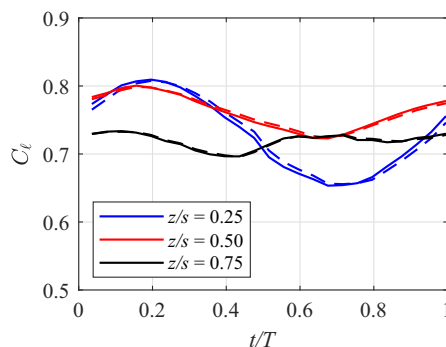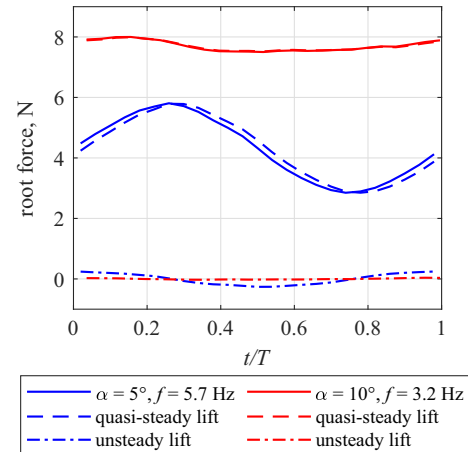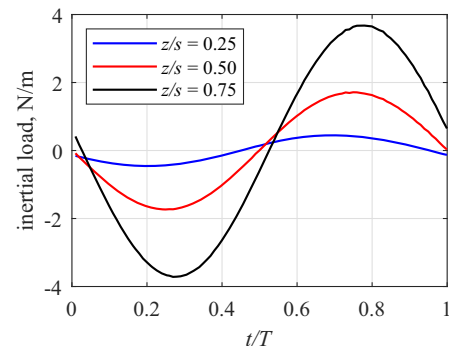

Fig. 31 Inertial loads at different spanwise locations for the gust with $f_g = 5.7$ Hz at $\alpha = 5$ deg.

Fig. 29 Unsteady lift (solid lines) and quasi-steady lift (dashed lines) over the period at $\alpha = 10$ deg for the gust with $f_g = 3.2$ Hz.
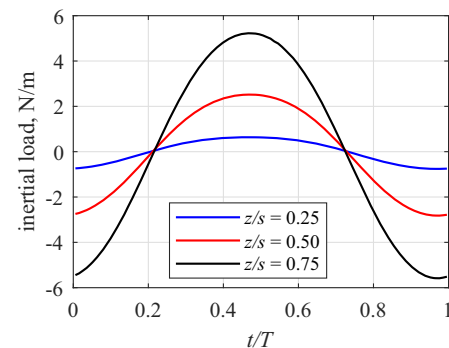

Fig. 32 Inertial loads at different spanwise locations for the gust with $f_g = 3.2$ Hz at $\alpha = 10$ deg.
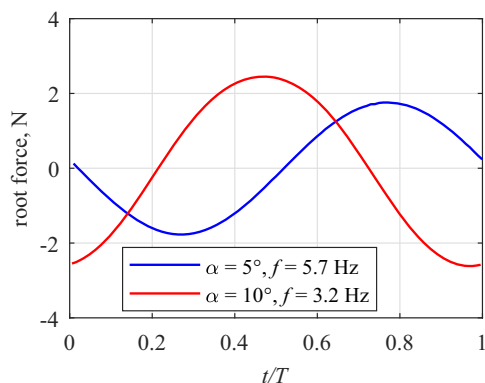
Fig. 33 Root force over the period resulting from the inertial load for both dynamic test cases.

period as a result of the phase lag differences in the wing dynamic response (see Table 3).

The root forces obtained with the integrated measurement approach in terms of the aerodynamic force and the sum of aerodynamic and inertial forces according to Eq. (5) are compared to the force balance measurements for the two dynamic test cases in Figs. 34 and 35, respectively. The dynamic behavior clearly differs between the two test cases. In the first case (Fig. 34), the inertial force nearly balances the dynamic variation of the aerodynamic force over the period such that the root force is approximately constant. In the second case (Fig. 35), a strong dynamic variation of the root force is observed, which is mainly contributed by the variation of the inertial force; whereas the aerodynamic force is approximately constant.
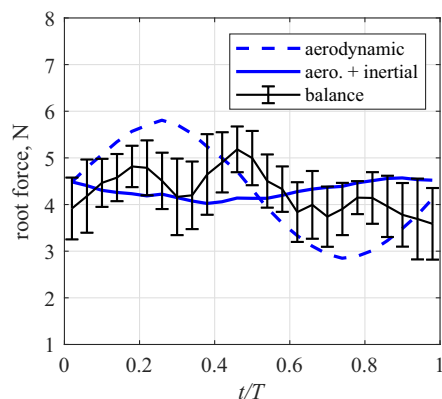

Fig. 34 Comparison of the root forces measured nonintrusively and with the balance for the gust with $f_g = 5.7$ Hz at $\alpha = 5$ deg (aero. denotes aerodynamic).
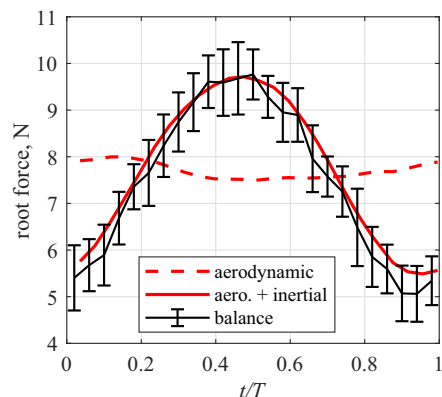

Fig. 35 Comparison of the root forces measured nonintrusively and with the balance for the gust with $f_g = 3.2$ Hz at $\alpha = 10$ deg.

A good agreement between the results from the integrated measurement approach and the force balance is observed in both dynamic test cases. The root mean square of the difference between the non-intrusive measurement and the force balance is 0.56 N for the gust with $f_g = 5.7$ Hz, which corresponds to 13.1% of the mean root force over the period measured with the force balance in this case. For the gust with $f_g = 3.2$ Hz, the root-mean-square difference between the measurements is 0.28 N, which corresponds to 3.8% of the mean root force measured with the balance. The differences between non-intrusive and balance measurements are mostly within the standard deviation of the balance measurements, which are indicated by error bars in the plots. The relatively larger differences between the force balance measurements and the nonintrusive measurements for the gust with $f_g = 5.7$ Hz are presumed to be produced by the higher-frequency contents of the structural response of the wing to the gust excitation because the wing was excited between the frequencies of the first and second bending modes (see Table 1). The higher-frequency content of the structural response is not present in the nonintrusive measurement due to the phase-averaging approach. However, even in this case, the root mean square of the difference between the two measurements is smaller than the standard deviation of the balance measurements from different acquisitions of the same test condition, which is 0.6N.

VI. Data Archive

The experimental data that are presented in this paper are available in a data archive of the 4TU.ResearchData center [48].

VII. Conclusions

In this study, the aeroelastic response of a highly flexible wing to steady and periodic unsteady inflows was determined experimentally in a wind-tunnel test. The wing that was investigated was the Delft–Pazy wing, which is an adaptation of the Pazy aeroelastic benchmark wing to be tested at lower freestream velocities. Two static test cases with different angles of attack and two dynamic test cases with different gust frequencies were considered. The measurements were performed with an integrated optical system, which provided Lagrangian particle tracking measurements of the wing motion via surface marker tracking and the flowfield around the wing by tracking the helium-filled soap bubble flow tracers. These measurements were postprocessed to obtain a reconstruction of the wing shape as well as the phase-averaged flowfield based on the measurements with a single system.

After the postprocessing of the measurements, the aerodynamic loads and (in the dynamic test cases) the inertial loads acting on the wing were determined through the application of physical models to the measured data. In the test cases with steady inflow, the obtained lift distributions were integrated along the span and compared to the reference measurements with a force balance, yielding excellent agreements with differences of around 1%. The analysis of the lift distribution on the wing during the periodic gust encounter revealed that for small wing deflections, the lift variation was sinusoidal and could thus be directly linked to the gust forcing; whereas for the dynamic test case with larger deflections, the temporal behavior of the lift varied, depending on the spanwise location. The results of the analysis of the unsteady aerodynamic and inertial loads were compared to force balance measurements in terms of the force at the root of the wing, yielding differences between around 4 and 13%. A potential reason for these remaining differences is the phase-averaging approach, which was used in this study to merge information from different measurement volumes, and thus inherently limited the temporal resolution of the measurement. A possible improvement in future studies would be the use of more cameras and light sources to capture the entire measurement volume instantaneously, thereby removing this limitation and allowing a more accurate nonintrusive aeroelastic characterization.

The results of the integrated measurement approach presented in this study provide insights into the static and dynamic aeroelastic response of a highly flexible wing at a level of detail that is

unattainable with conventional measurement approaches that are based on installed sensors. Particularly relevant are the measurements of the lift distributions along the entire span during the gust encounter, which are useful for the validation of the unsteady aerodynamic models implemented in aeroelastic simulation tools. The use of a single measurement system for aerodynamic and structural measurements simplifies the experimental setup and data processing as compared to the coordinated use of multiple measurement systems, which makes the approach presented in this study a promising method for producing experimental reference data for dynamic aeroelastic problems of different kinds in the future, such as limit-cycle oscillations. The determination of the drag force from nonintrusive flowfield measurements is important for such oscillations and other large-amplitude scenarios, and it will be investigated in such future studies.

Appendix: Measurements of the Gust Inflow

The variation of the transversal velocity component $v(t)$ in the inflow due to the operation of the gust generator has been estimated based on the ensemble-averaged LPT flowfield measurements. To minimize the interaction between the wing and the gust, the gust inflow is analyzed upstream of the wing at the streamwise location of $x/c = -0.75$, which corresponds to the upstream edge of the field of view of the LPT system. To obtain the gust inflow measurements, the phase-averaged measurements of the transversal velocity component at the considered streamwise location are averaged over an area that is centered at midspan of the deflected wing and spans $0.5s$ in the spanwise direction and $0.4s$ in the transversal direction for each of the 25 phase instants. At the considered streamwise location, the influence of the wing on the transversal flow velocity is nonzero; therefore, the transversal velocity is given as the sum of the contributions of the gust and the velocity induced by the wing: $v(t) = v_{\text{gust}}(t) + v_{\text{wing}}(t)$. To determine the gust velocity only, it is assumed that the velocity induced by the wing at $x/c = -0.75$ does not vary strongly over time such that $v_{\text{gust}}(t) \approx v(t) - \overline{v(t)}$. The transversal gust velocity measurements obtained with this approximation are shown in Fig. A1 for the gust with a frequency of $f = 5.7$ Hz and in Fig. A2 for the gust with a frequency of $f = 3.2$ Hz. The measurements for both gusts are well approximated with a sinusoidal fit that uses the inverse of the gust frequency as the period length. Operating the gust generator at the higher frequency of $f = 5.7$ Hz produces gust measurements with a transversal velocity amplitude of $\hat{v}_{\text{gust}} = 0.81$ m $\cdot$ s^{-1} that is around 20% larger than the value of $\hat{v}_{\text{gust}} = 0.65$ m $\cdot$ s^{-1} that is obtained for the lower frequency of $f = 3.2$ Hz. The sinusoidal fits to the gust measurements are used to align the gusts in time throughout the paper such that, for both gust frequencies, the time instant $t/T = 0$ corresponds to the time instant at which the gust arrives at the theoretical aerodynamic center of the wing at $x/c = 0.25$, based on the assumption that the gust convects downstream from the measurement location with the freestream velocity.
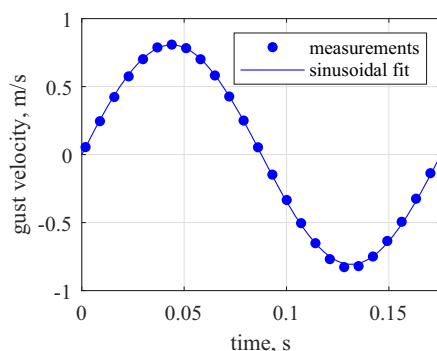
Fig. A1   Measurements of the transversal gust velocity with a sinusoidal fit for the gust with a frequency of $f = 5.7$ Hz.
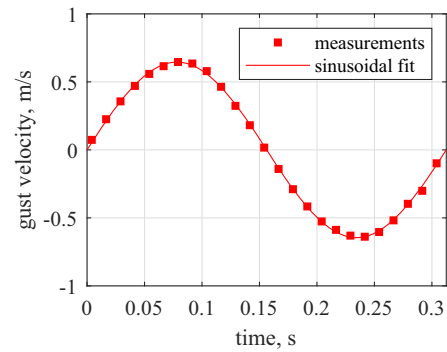
Fig. A2   Measurements of the transversal gust velocity with a sinusoidal fit for the gust with a frequency of $f = 3.2$ Hz.

References

[1] Dimitriadis, G., *Introduction to Nonlinear Aeroelasticity*, Wiley, Hoboken, NJ, 2017.

[2] Wu, Z., Cao, Y., and Ismail, M., "Gust Loads on Aircraft," *Aeronautical Journal*, Vol. 123, No. 1266, 2019, pp. 1216–1274.
https://doi.org/10.1017/aer.2019.48

[3] Bernhammer, L. O., de Breuker, R., and Karpel, M., "Geometrically Nonlinear Structural Modal Analysis Using Fictitious Masses," *AIAA Journal*, Vol. 55, No. 10, 2017, pp. 3584–3593.
https://doi.org/10.2514/1.J054787

[4] Kantor, E., Raveh, D. E., and Cavallaro, R., "Nonlinear Structural, Nonlinear Aerodynamic Model for Static Aeroelastic Problems," *AIAA Journal*, Vol. 57, No. 5, 2019, pp. 2158–2170.
https://doi.org/10.2514/1.J057309

[5] Drachinsky, A., and Raveh, D. E., "Modal Rotations: A Modal-Based Method for Large Structural Deformations of Slender Bodies," *AIAA Journal*, Vol. 58, No. 7, 2020, pp. 3159–3173.
https://doi.org/10.2514/1.J058899

[6] Tang, D., and Dowell, E. H., "Experimental and Theoretical Study on Aeroelastic Response of High-Aspect-Ratio Wings," *AIAA Journal*, Vol. 39, No. 8, 2001, pp. 1430–1441.
https://doi.org/10.2514/2.1484

[7] Tang, D., and Dowell, E. H., "Experimental and Theoretical Study of Gust Response for High-Aspect-Ratio Wing," *AIAA Journal*, Vol. 40, No. 3, 2002, pp. 419–429.
https://doi.org/10.2514/2.1691

[8] Tang, D., and Dowell, E. H., "Limit-Cycle Hysteresis Response for a High-Aspect-Ratio Wing Model," *Journal of Aircraft*, Vol. 39, No. 5, 2002, pp. 885–888.
https://doi.org/10.2514/2.3009

[9] Avin, O., Raveh, D. E., Drachinsky, A., Ben-Shmuel, Y., and Tur, M., "Experimental Aeroelastic Benchmark of a Very Flexible Wing," *AIAA Journal*, Vol. 60, No. 3, 2022, pp. 1745–1768.
https://doi.org/10.2514/1.J060621

[10] Drachinsky, A., Avin, O., Raveh, D. E., Ben-Shmuel, Y., and Tur, M., "Flutter Tests of the Pazy Wing," *AIAA Journal*, Vol. 60, No. 9, 2022, pp. 5414–5421.
https://doi.org/10.2514/1.J061717

[11] Riso, C., and Cesnik, C. E., "Correlations Between UM/NAST Nonlinear Aeroelastic Simulations and the Pre-Pazy Wing Experiment," *AIAA SciTech 2021 Forum*, AIAA Paper 2021-1721, 2021.
https://doi.org/10.2514/6.2021-1712

[12] Riso, C., and Cesnik, C. E., "Low-Order Geometrically Nonlinear Aeroelastic Modeling and Analysis of the Pazy Wing Experiment,"

AIAA SciTech 2022 Forum, AIAA Paper 2022-2313, 2022.
https://doi.org/10.2514/6.2022-2313

[13] Hilger, J., and Ritter, M. R., "Nonlinear Aeroelastic Simulations and Stability Analysis of the Pazy Wing Aeroelastic Benchmark," *Aerospace*, Vol. 8, No, 10, 2021, Paper 308.
https://doi.org/10.3390/aerospace8100308

[14] Goizueta, N., Wynn, A., Palacios, R., Drachinsky, A., and Raveh, D. E., "Flutter Predictions for Very Flexible Wing Wind Tunnel Test," *Journal of Aircraft*, Vol. 59, No, 4, 2022, pp. 1082–1097.
https://doi.org/10.2514/1.C036710

[15] Collar, A. R., "The Expanding Domain of Aeroelasticity," *Aeronautical Journal*, Vol. 50, No. 428, 1946, pp. 613–636.
https://doi.org/10.1017/S0368393100120358

[16] Tang, D., and Dowell, E. H., "Experimental Aeroelastic Models Design and Wind Tunnel Testing for Correlation with New Theory," *Aerospace*, Vol. 3, No. 2, 2016, Paper 12.
https://doi.org/10.3390/aerospace3020012

[17] Liu, T., Burner, A. W., Jones, T. W., and Barrows, D. A., "Photogrammetric Techniques for Aerospace Applications," *Progress in Aerospace Sciences*, Vol. 54, Oct. 2012, pp. 1–58.
https://doi.org/10.1016/j.paerosci.2012.03.002

[18] Raffel, M., Willert, C. E., Scarano, F., Kähler, C. J., Wereley, S. T., and Kompenhans, J., *Particle Image Velocimetry: A Practical Guide*, Springer, New York, 2018.

[19] Gherlone, M., Cerracchio, P., and Mattone, M., "Shape Sensing Methods: Review and Experimental Comparison on a Wing-Shaped Plate," *Progress in Aerospace Sciences*, Vol. 99, May 2018, pp. 14–26.
https://doi.org/10.1016/j.paerosci.2018.04.001

[20] van Oudheusden, B. W., "PIV-Based Pressure Measurement," *Measurement Science and Technology*, Vol. 24, No. 3, 2013, Paper 032001.
https://doi.org/10.1088/0957-0233/24/3/032001

[21] Rival, D. E., and van Oudheusden, B. W., "Load-Estimation Techniques for Unsteady Incompressible Flows," *Experiments in Fluids*, Vol. 58, No. 3, 2017, Paper 20.
https://doi.org/10.1007/s00348-017-2304-3

[22] Liu, T., Montefort, J., Gregory, J., Palluconi, S., Crafton, J., and Fonov, S., "Wing Deformation Measurements from Pressure Sensitive Paint Images Using Videogrammetry," *41st AIAA Fluid Dynamics Conference and Exhibit*, AIAA Paper 2011-3725, 2011.
https://doi.org/10.2514/6.2011-3725

[23] Giovannetti, L. M., Banks, J., Turnock, S. R., and Boyd, S. W., "Uncertainty Assessment of Coupled Digital Image Correlation and Particle Image Velocimetry for Fluid-Structure Interaction Wind Tunnel Experiments," *Journal of Fluids and Structures*, Vol. 68, Jan. 2017, pp. 125–140.
https://doi.org/10.1016/j.jfluidstructs.2016.09.002

[24] Zhang, P., Peterson, S. D., and Porfiri, M., "Combined Particle Image Velocimetry/Digital Image Correlation for Load Estimation," *Experimental Thermal and Fluid Science*, Vol. 100, Jan. 2019, pp. 207–221.
https://doi.org/10.1016/j.expthermflusci.2018.09.011

[25] Schanz, D., Gesemann, S., and Schröder, A., "Shake-the-Box: Lagrangian Particle Tracking at High Particle Image Densities," *Experiments in Fluids*, Vol. 57, No. 5, 2016, Paper 70.
https://doi.org/10.1007/s00348-016-2157-1

[26] Mertens, C., Sciacchitano, A., van Oudheusden, B. W., and Sodja, J., "An Integrated Measurement Approach for the Determination of the Aerodynamic Loads and Structural Motion for Unsteady Airfoils," *Journal of Fluids and Structures*, Vol. 103, May 2021, Paper 103293.
https://doi.org/10.1016/j.jfluidstructs.2021.103293

[27] Mertens, C., de Rojas Cordero, T., Sodja, J., Sciacchitano, A., and van Oudheusden, B. W., "Aeroelastic Characterization of a Flexible Wing Using Particle Tracking Velocimetry Measurements," *AIAA Journal*, Vol. 60, No. 1, 2022, pp. 276–286.
https://doi.org/10.2514/1.J060713

[28] Drela, M., "XFOIL: An Analysis and Design System for Low Reynolds Number Airfoils," *Low Reynolds Number Aerodynamics*, edited by T. J. Mueller, Vol. 54, Lecture Notes in Engineering, Springer, New York, 1989.
https://doi.org/10.1007/978-3-642-84010-4_1

[29] Anderson, J. D., Jr., *Fundamentals of Aerodynamics*, 5th ed., McGraw–Hill, New York, 2011, pp. 282–284.

[30] Mertens, C., Costa Fernández, J. L., Sciacchitano, A., van Oudheusden, B. W., and Sodja, J., "Gridless Determination of Aerodynamic Loads Using Lagrangian Particle Tracks," *14th International Symposium on Particle Image Velocimetry*, Illinois Inst. of Technology - Paul V. Galvin Library, Chicago, 2021.
https://doi.org/10.18409/ispiv.v1i1.82

[31] Sharma, S. D., and Deshpande, P. J., "Kutta–Joukowsky Theorem in Viscous and Unsteady Flow," *Experiments in Fluids*, Vol. 52, No. 6, 2012, pp. 1581–1591.
https://doi.org/10.1007/s00348-012-1276-6

[32] Olasek, K., and Karczewski, M., "Velocity Data-Based Determination of Airfoil Characteristics with Circulation and Fluid Momentum Change Methods, Including a Control Surface Size Independence Test," *Experiments in Fluids*, Vol. 62, No. 5, 2021, Paper 108.
https://doi.org/10.1007/s00348-021-03193-9

[33] Theodorsen, T., "General Theory of Aerodynamic Instability and the Mechanism of Flutter," NACA TR-496, 1949.

[34] Katz, J., and Plotkin, A., *Low-Speed Aerodynamics*, 2nd ed., Cambridge Univ. Press, Cambridge, England, U.K., 2001, p. 394.

[35] Jaworski, J. W., and Dowell, E. H., "Comparison of Theoretical Structural Models with Experiment for a High-Aspect-Ratio Aeroelastic Wing," *Journal of Aircraft*, Vol. 46, No. 2, 2009, pp. 708–713.
https://doi.org/10.2514/1.39244

[36] Pastor, M., Binda, M., and Harčarik, T., "Modal Assurance Criterion," *Procedia Engineering*, Vol. 48, Nov. 2012, pp. 543–548.
https://doi.org/10.1016/j.proeng.2012.09.551

[37] Lancelot, P. M. G. J., Sodja, J., Werter, N. P. M., and De Breuker, R., "Design and Testing of a Low Subsonic Wind Tunnel Gust Generator," *Advances in Aircraft and Spacecraft Science*, Vol. 4, No. 2, 2017, pp. 125–144.
https://doi.org/10.12989/aas.2017.4.2.125

[38] Leishman, G. J., *Principles of Helicopter Aerodynamics*, Cambridge Univ. Press, Cambridge, England, U.K., 2006, p. 427.

[39] Scarano, F., Ghaemi, S., Caridi, G. C. A., Bosbach, J., Dierksheide, U., and Sciacchitano, A., "On the Use of Helium-Filled Soap Bubbles for Large-Scale Tomographic PIV in Wind Tunnel Experiments," *Experiments in Fluids*, Vol. 56, No. 2, 2015, Paper 42.
https://doi.org/10.1007/s00348-015-1909-7

[40] Faleiros, D. E., Tuinstra, M., Sciacchitano, A., and Scarano, F., "Generation and Control of Helium-Filled Soap Bubbles for PIV," *Experiments in Fluids*, Vol. 60, No. 3, 2019, Paper 40.
https://doi.org/10.1007/s00348-019-2687-4

[41] Wieneke, B., "Volume Self-Calibration for 3D Particle Image Velocimetry," *Experiments in Fluids*, Vol. 45, No. 4, 2008, pp. 549–556.
https://doi.org/10.1007/s00348-008-0521-5

[42] Schanz, D., Gesemann, S., Schröder, A., Wieneke, B., and Novara, M., "Non-Uniform Optical Transfer Functions in Particle Imaging: Calibration and Application to Tomographic Reconstruction," *Measurement Science and Technology*, Vol. 24, No. 2, 2012, Paper 024009.
https://doi.org/10.1088/0957-0233/24/2/024009

[43] Sciacchitano, A., and Scarano, F., "Elimination of PIV Light Reflections via a Temporal High Pass Filter," *Measurement Science and Technology*, Vol. 25, No. 8, 2014, Paper 084009.
https://doi.org/10.1088/0957-0233/25/8/084009

[44] Mitrotta, F. M. A., Sodja, J., and Sciacchitano, A., "On the Combined Flow and Structural Measurements via Robotic Volumetric PTV," *Measurement Science and Technology*, Vol. 33, No. 4, 2022, Paper 045201.
https://doi.org/10.1088/1361-6501/ac41dd

[45] Jux, C., Sciacchitano, A., Schneiders, J. F., and Scarano, F., "Robotic Volumetric PIV of a Full-Scale Cyclist," *Experiments in Fluids*, Vol. 59, No. 4, 2018, Paper 74.
https://doi.org/10.1007/s00348-018-2524-1

[46] Weaver, W., Jr., Timoshenko, S. P., and Young, D. H., *Vibration Problems in Engineering*, Wiley, New York, 1991.

[47] Agüera, N., Cafiero, G., Astarita, T., and Discetti, S., "Ensemble 3D PTV for High Resolution Turbulent Statistics," *Measurement Science and Technology*, Vol. 27, No. 12, 2016, Paper 124011.
https://doi.org/10.1088/0957-0233/27/12/124011

[48] Mertens, C., and Sodja, J., Delft–Pazy Wing Data Archive (online database), 4TU.Research DataCollection, Delft Univ. of Technology Library, Delft, The Netherlands, 2022.
https://doi.org/10.4121/c.5720456

A. R. Jones
Associate Editor